ABSTRACT

Title of dissertation: DEVELOPMENT OF A SPATIALLY CONTROLLABLE CHEMICAL VAPOR DEPOSITION SYSTEM

Jae-Ouk Choo, Doctor of Philosophy, 2005

Dissertation directed by: Professor Raymond A. Adomaitis
Department of Chemical Engineering

Most conventional chemical vapor deposition (CVD) systems do not have the spatial actuation and sensing capabilities necessary to control deposition uniformity, or to intentionally induce nonuniform deposition patterns for single-wafer combinatorial CVD experiments. In an effort to address these limitations, a novel CVD reactor system has been developed that can explicitly control the spatial profile of gas-phase chemical composition across the wafer surface. In this thesis, the simulation-based design of a prototype reactor system and the results of preliminary experiments performed to evaluate the performance of the prototype in depositing tungsten films are presented. Initial experimental results demonstrate that it is possible to produce spatially patterned wafers using a CVD process by controlling gas phase reactant composition. Based on the evaluation of the first prototype, a second prototype system was designed and constructed, enabling for greater control and programmability. The capability of this prototype for performing combinatorial CVD experiments is discussed. Finally, improvement of intra-segment uniformity

and film thickness together with micro structure or composition is discussed.

DEVELOPMENT OF A SPATIALLY CONTROLLABLE CHEMICAL VAPOR DEPOSITION SYSTEM

by

Jae-Ouk Choo

Dissertation submitted to the Faculty of the Graduate School of the
University of Maryland, College Park in partial fulfillment
of the requirements for the degree of
Doctor of Philosophy
2005

Advisory Commmittee:

Professor Raymond A. Adomaitis, Chair/Advisor
Professor Kyu Yong Choi
Professor Panagiotis Dimitrakopoulos
Professor Gary W. Rubloff
Professor Evanghelos Zafiriou

TABLE OF CONTENTS

LIST OF TABLES

LIST OF FIGURES

Chapter 1

The Concept of Spatially Controllable Chemical Vapor Deposition System

1.1 Introduction

Chemical Vapor Deposition (CVD) is one of the essential unit operations in semiconductor manufacturing because of its ability to deposit thin smooth films conformally onto submicron-scale features. CVD processes have evolved together with the semiconductor industry, from early bell-jar CVD reactors to current cold-wall single-wafer reactors [1]. The continuing reduction of device feature size, growing scale of device integration, expanding number of new electronic materials, and increasing substrate (wafer) size motivate development of the new CVD processes necessary to sustain the advancement of microelectronic technology. However, current equipment designs are aimed at specific deposition processes and operating conditions (e.g., pressures, chemical species, flows, temperatures) with the design goal of producing process uniformity across large wafers (300 mm diameter, resulting in hundreds of semiconductor chips) at the nominal design conditions. Optimizing a design to CVD and other manufacturing equipment for a specific range of design conditions has a number of fundamental shortcomings:

1. Semiconductor manufacturing processes change rapidly in time (e.g., relative to typical petrochemical processes). Because technology improvements must be implemented incrementally to maintain or improve yields in complex, multi-step wafer production sequences, a new generation of process equipment tech-

nology may only emerge after several of these improvement steps.

2. Process conditions for optimal material and device quality often do not meet the across-wafer uniformity requirements for manufacturing, forcing a tradeoff between product performance and manufacturing productivity.

3. Fundamental chemical and physical mechanisms for semiconductor processes are often not well known, so that it is difficult to identify *a priori* the best design which balances the demands of product performance and manufacturing uniformity.

4. Experimentation for process optimization is expensive, requiring sets of runs to investigate and characterize complex process behavior.

1.2 Equipment Design for Uniformity

Current CVD reactor designs typically consist of a cooled-wall reaction (vacuum) chamber in which one to several wafers are processed. Energy needed to drive the deposition reactions is provided by an inductively-heated susceptor or a wafer stage heated by external lamps or electrical resistance heating. Reactant gases enter the reaction chamber through a gas delivery system, flow over the wafer(s), and the residual gas is pumped out through the chamber exhaust port. Because of the importance of spatially uniform (across-wafer) processing capabilities, showerhead designs for gas delivery to the wafer typically incorporate a high density of uniformly spaced small holes in an attempt to distribute gas flow as uniformly as possible across a large diameter wafer. In addition, reactor design components in-

cluding chamber, wafer position (and rotation), pumping, heating, and gas inlet are commonly structured to achieve high uniformity with cylindrical symmetry about the wafer.

Significant research effort has been directed towards improving growth uniformity of CVD process. Early experimental and simulation-based process equipment research focused on developing an understanding of the important transport and reaction mechanisms of CVD processes and devising optimization methods to aid process parameter selection. For example, Wang, Gorves, Palmateer, Weyburne and Brown [2] used flow visualization techniques to show that heated wafers can disturb gas flow patterns; their experiments suggested lowering operation pressures to reduce the perturbation. Moffat and Jensen [3] demonstrated the utility of simulation technology for process optimization in the context of a horizontal Si homoepitaxial deposition reactor. Their simulation study examined the relationship between the growth uniformity and tilt angle of the susceptor, giving the optimal setting for this reactor geometry parameter. Another example of rigorous modeling and simulation was performed by Kleijn, van der Meer and Hoogendoorn [4]. Their mathematical model was used to show the significance of thermal diffusion and its effect on growth uniformity and gas-phase reactant species distribution.

The evolution of CVD reactor designs also has been motivated by the need to improve growth uniformity. For example, various showerhead designs have been developed to generate uniform gas flow patterns over the wafer surface [5] [2] or to produce uniform film deposition rates [6] [7]. Still more advanced design features are found in the annular, three-zone Texas Instruments showerhead [8] for tungsten

and other CVD processes, where individual gas mass flow controllers could be used to set the gas flow rate to each segment.

In some MOCVD processes, the separation of gas precursors is critical because highly reactive gas precursors can cause undesirable gas phase reactions. In an effort to reduce gas phase reactions, Van der Stricht, Moerman, Demeester, Crawley and Thush [9] developed a vertical reactor with separate feed ports for each precursor species, and experiments revealed the relationship between the wafer rotation rate and thickness uniformity of GaN and InGaN films. Another example of using separate gas injectors for individual precursors can be found in the horizontal flow MOCVD reactor introduced by Yang, Huang, Chi and Wu [10]. Theodoropoulos, Mountziaris, Moffat and Han [11] described a new MOCVD reactor design of featuring an annular-ring showerhead configuration that allowed the controlled injection of separate precursors. Several annular ring designs were evaluated in that study, and as with Van der Stricht and Yang, Theodoropoulos and co-workers concluded that novel gas delivery designs offered new operational degrees of freedom with which uniformity could be controlled; they also pointed to the importance of simulation tools in selecting optimized operating conditions.

CVD reactor designs have been developed specifically to allow or improve active control of wafer processing conditions during the dynamic processing cycle. For example, work at TI [12] exploited multiple (3 and 4) heating zones radially across the wafer in single-wafer rapid thermal processing to achieve temperature uniformity. That approach has been incorporated into commercial RTP equipment, e.g., from CVC Products, Inc., and from Applied Materials. The SEMATECH

testbed RTP system [13] and the three-zone RTP system at North Carolina State University [14] exploit independent lamp zones for edge-cooling compensation and dynamic uniformity control. Further developments in this area include reduced-model-based real-time control studies of the three-zone NCSU RTP system [15] [16] and reduced-model-based order state estimation and optimal control of a horizontal high-pressure CVD system [17] [18] [19].

1.3 The Programmable Reactor Concept

The existing design strategy of semiconductor CVD manufacturing equipment faces fundamental barriers limiting the development of next-generation reactor systems; there is a need for a new design paradigm to: (1) decouple fundamental materials and product quality requirements from across-wafer uniformity in manufacturing, so that both may be achieved simultaneously; (2) accelerate materials and process learning and optimization; and (3) develop equipment that is flexible and scalable to succeeding generations of the technology.

As a response to these perceived CVD reactor design shortcomings, this thesis presents the development of a novel CVD reactor intended to improve across-wafer 2-dimensional controllability. This new CVD reactor introduces a segmented showerhead design featuring individually controllable gas distribution actuators, a design that reverses the residual gas flow by directing it up through the showerhead, and sampling ports for in-situ gas sampling (Figure 1.1). This thesis describes the development of this novel design concept by simulation, a sequence of experiments performed using a prototype reactor, and the interpretation of preliminary exper-

imental data by comparison with results of simulation and parameter estimation methods to demonstrate the validity of the design principles.

This design is referred to as the Programmable CVD Reactor concept because of the potential real-time control of gas phase composition across the wafer surface has for making possible novel operating modes. For example, this reactor design will enable single-wafer combinatorial experiments in which different materials can be created or different process conditions can be tested in a single experiment, producing the library wafer illustrated in Figure 1.2. In subsequent deposition runs, the reactor then can be reprogrammed to produce uniform films corresponding to one point on the library wafer without making any hardware adjustments. This mode of operation is made possible by the combination of the flexible design of the Programmable Reactor and model-based interpretation of the sensor and metrology data collected during the processing of the library wafer.

1.4 **Reactor Design Principles**

A common feature of all the CVD systems discussed in the previous section having the capability of controlling spatial variations in gas composition leaving the showerhead (e.g.,[8] [11]) is that the actuation capabilities are limited to 1-dimensional control in the radial direction. Furthermore, a characteristic common to these designs is the segment-to-segment interaction produced by the net flow of reactant gas across the wafer to the reactor chamber exhaust. For example, consider the simulation results presented in Figure 1.3; this simulation depicts the behavior of a showerhead 0.1 m in diameter ($100mm$ wafer) with a $0.01m$ gap between the shower-

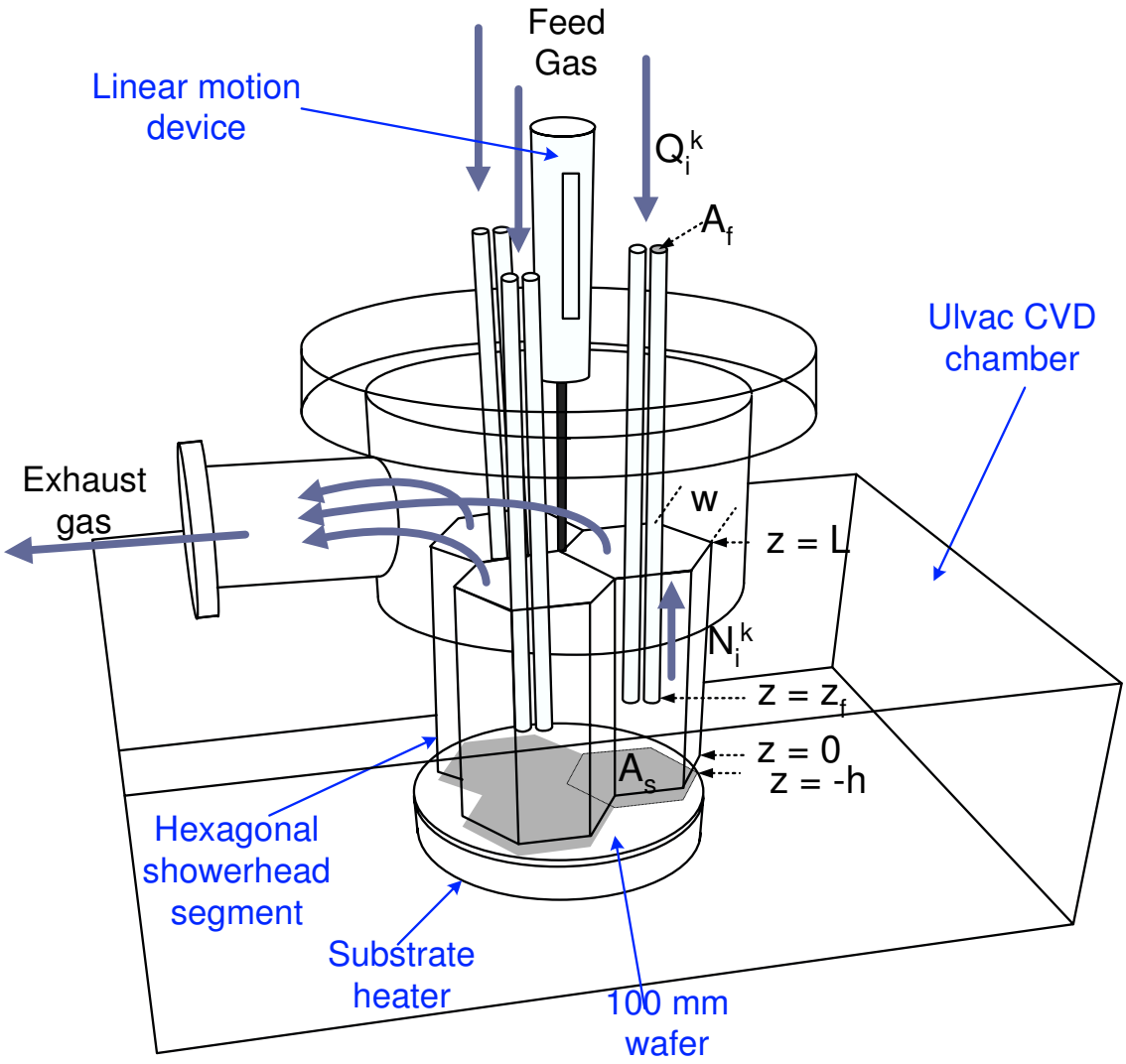

Figure 1.1: A schematic diagram of the Programmable CVD Reactor three-zone prototype showing the segmented showerhead structure, segment feed and sampling lines, linear motion device, and notation used in developing the simulator.

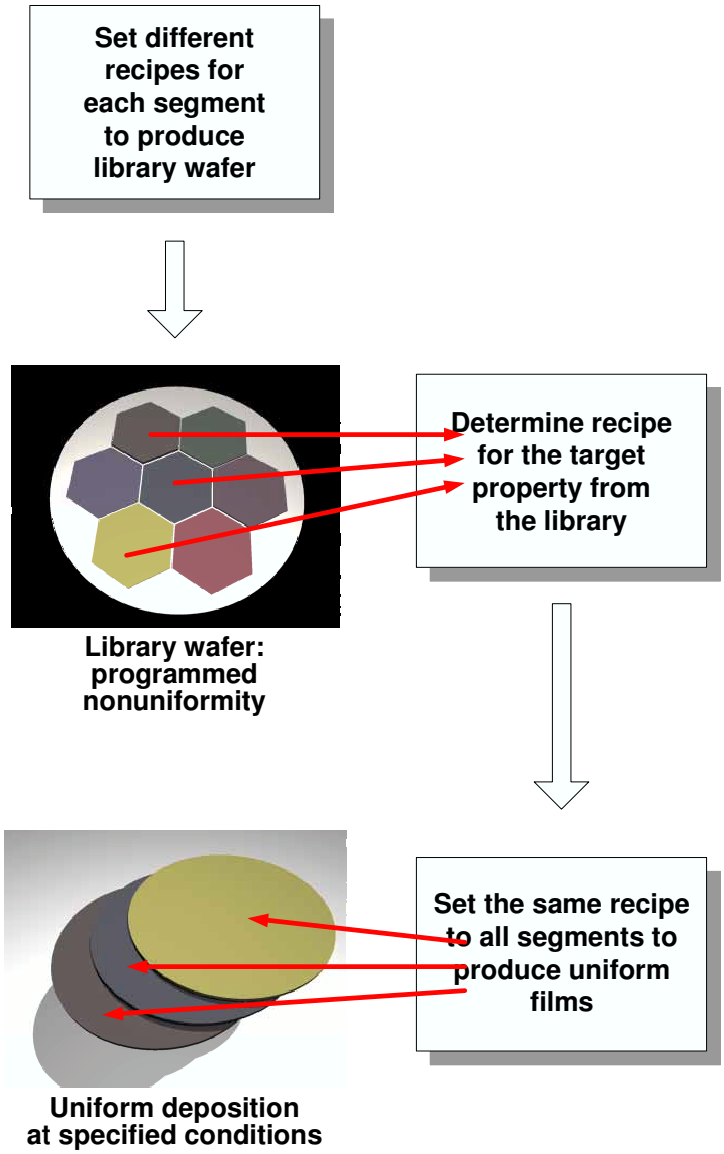

Figure 1.2: A rapid process prototyping approach to new materials and process development. The spatial patterning capabilities of the Programmable CVD Reactor can be used to produce a "library" wafer (left) containing regions of distinct material properties; the reactor system then can be reprogrammed to deposit spatially uniform films of the chosen property (right).

head and wafer surface. Gas flow to each segment is set to $20sccm$ and consists of H_2 at $623K$ and $5torr$, representative operating conditions for W CVD processes. The concentration of WF_6 in the middle segment is set at $1wt$ % in H_2. The equations describing the steady-state gas flow were solved using a global spectral discretization technique where the basis functions correspond to eigenfunctions of heat equation in cylindrical coordinates. In this solution approach, the discretized momentum balance equations are solved iteratively for the two velocity components for a given pressure field; this velocity field is substituted into the continuity equation to define a residual function which is minimized in a Galerkin procedure by projecting the residual function onto the pressure field basis functions. The WF_6 species balance equation likewise is discretized and solved iteratively using a Galerkin projection method and a Jacobian-free formulation of a Krylov-subspace iterative procedure. Converged solutions were found using fewer than 50 basis functions in each of the directions.

Using this simulation approach, one can observe that when carrier gas is injected through the center and outer annular region, and the deposition precursor species are injected through the middle annular injection port, the net convection across the wafer shifts the region where the precursor plume interacts with the wafer surface downstream relative to the injection point (Figure 1.3, top). Therefore, the net flux across the wafer surface, inherent in the annual segmented showerhead designs, reduces the ability to accurately control gas phase composition at the wafer surface (Figure 1.3, bottom).

As an alternative to reactor systems based on the annular segmented show-

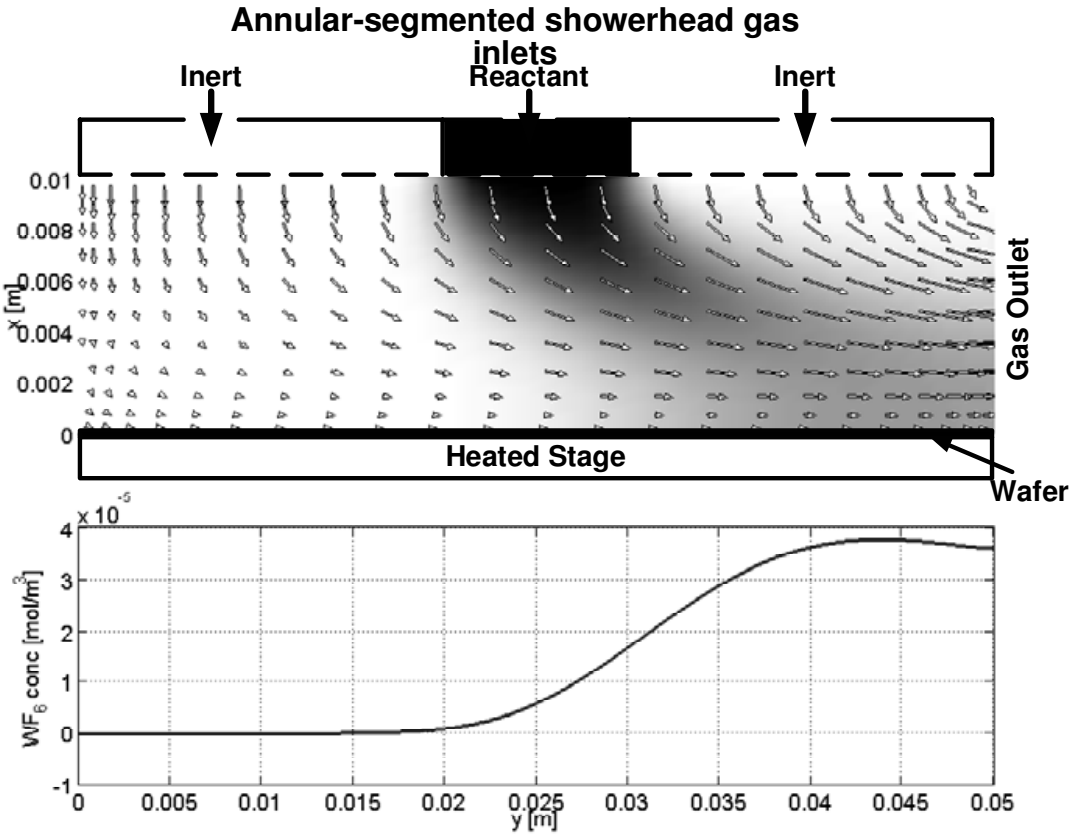

Figure 1.3: Gas concentration field computed for a segmented showerhead design illustrating the mismatch between gas injector location (top) and the resulting gas concentration profile over the wafer surface (bottom) in a non-reverse flow design.

erhead design, the Programmable Reactor system incorporates three new design features to improve the spatial control of gas phase composition. The first is the development of a showerhead design consisting of an assembly of hexagonal showerhead sub-elements (segments) arrayed across the wafer surface. The reactant gas composition and feed rate is controllable within each segment, resulting in true 2-dimensional control of gas composition across the wafer. The spatial resolution with which gas phase composition can be controlled is determined by the size of showerhead segments.

The second new design feature is the recirculation of residual gas up through each segment of the showerhead; exhaust gases mix in a common exhaust volume above the showerhead honeycomb structure (Figure 1.1). When the total volumetric flow rate and other properties of feed gas to each segment are equal, the effect of this design feature is to create periodic flow fields in the gap region between the bottom of the showerhead assembly and the wafer surface (Figure 1.4). In this simulation result it is possible to see that the boundaries of the periodic flow field match the segment wall locations, indicating that there will be no convective flux of reactant species between the segment regions, eliminating the problems generated by drawing exhaust gas across the wafer surface.

This simulation represents three segments in a linear arrangement with $20 sccm$ flow of H_2 to each; the simulation is limited to the gap region and does not take into account back-diffusion from the common exhaust volume. As in the simulation of the annular segmented showerhead design, the center segment also includes $1 wt\%$ WF_6. Each segment has a diameter of $0.05m$, and each feed tube has a radius of

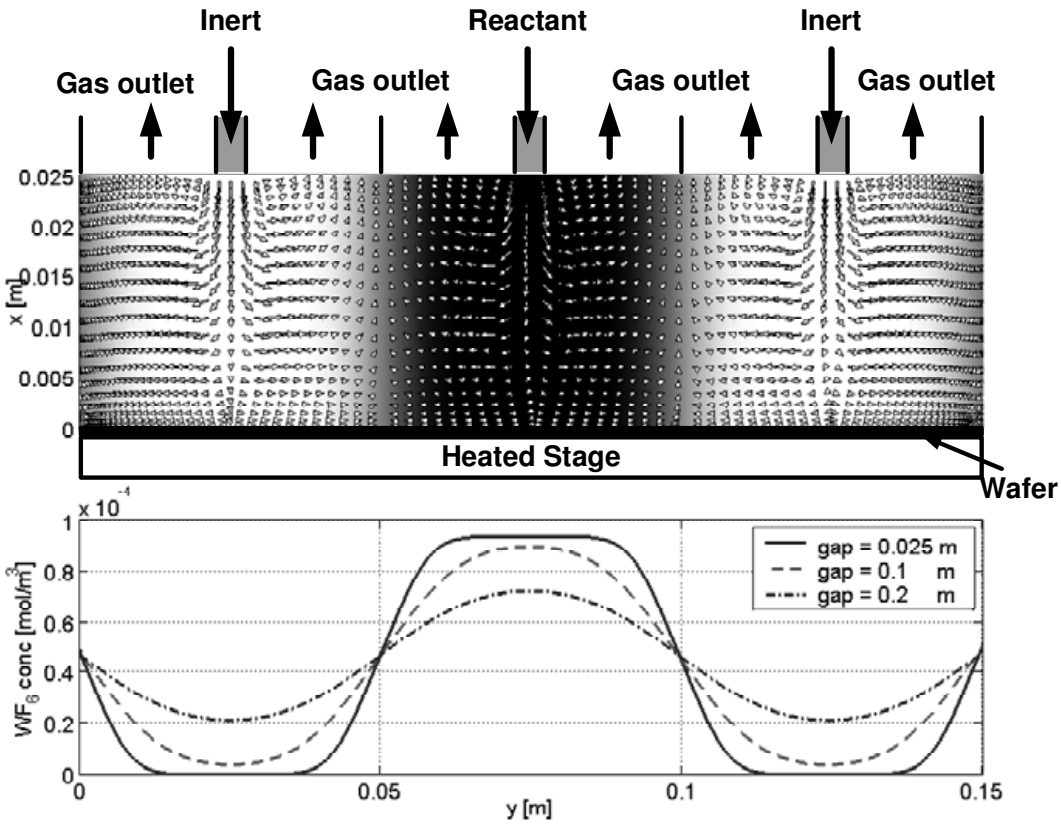

Figure 1.4: Periodic flow patterns and gas concentration field generated by a three segment, reverse-flow showerhead design (top) and resulting concentration profiles across the wafer as a function of gap size (bottom).

$0.005m$. As in the annular design, $T = 623K$ and the total pressure was set to $5torr$. The numerical solution procedure for computing the gas velocity and composition fields, based on a global spectral projection method, is identical to that described for the annular geometry reactor.

The third new design feature of the Programmable Reactor is the ability to manipulate the showerhead/wafer gap size. Small gap settings will reduce inter-segment diffusion in the gap region leading to deposition of distinct hexagonal patterns; increasing the gap size will spread the pattern, ultimately producing smooth concentration gradients across the wafer surface when reactant gas composition varies from segment-to-segment. An example of the smooth concentration gradients across the wafer surface that can be produced in this manner is shown in the simulation results depicted in Figure 1.4, where the across-wafer concentration profile of the WF_6 reactant species is shown.

Elimination of inter-segment region convective transport in the gap improves the accuracy with which gas composition can be controlled across the wafer surface because across-wafer transport will be governed solely by diffusion. Likewise, the accuracy of simulators used to interpret deposition data will be enhanced, improving the ability to correlate process operating conditions with film properties at all points on the library wafer. Because of the potential for accurately predicting the continuous variation of gas phase concentration across the wafer surface, it may be possible to generate library wafers with continuously graded characteristics across the wafer surface, increasing the information that can be obtained from a single deposition run. The system then can be run with closer showerhead-wafer spacing to produce a

finite number of hexagonal patches of material selected from the first library wafer, to provide a more accurate assessment of the process conditions needed to produce the desired material.

Chapter 2

Preliminary Experiments and Simulations with Prototype System P1

2.1 Introduction : Prototype Construction

To test the feasibility of the Programmable CVD concept, a prototype reactor was designed and constructed by modifying one reaction chamber of an Ulvac-ERA1000 CVD cluster tool. The Ulvac cluster tool located on the University of Maryland's campus is a commercial CVD system used for selective tungsten (W) deposition. W CVD, used to form vertical interconnects in VLSI and ULSI circuits, represents a relatively mature, but commercially important, manufacturing process [20], and so was chosen for evaluating the engineering design of the programmable reactor. While W CVD deposition mechanisms and reactor systems have been studied extensively (e.g., [21] [22] [23] [24], open process development issues remain. Even in the simplest case of blanket deposition using H_2 and WF_6, the reactant/reducing gas ratio and WF_6 gas concentration result in two operational degrees of freedom that force a tradeoff between film conformality and deposition rate, where the latter is compounded by reactor design factors that determine where the transition from reaction rate to mass-transfer limited operation takes place.

In its original configuration, the hydrogen reducing gas entered through a quartz showerhead above the wafer; wafer heating was provided by a ring of heating lamps above the showerhead. As part of the Programmable Reactor modifications, substrate heating was used in place of lamp heating, and the quartz showerhead was

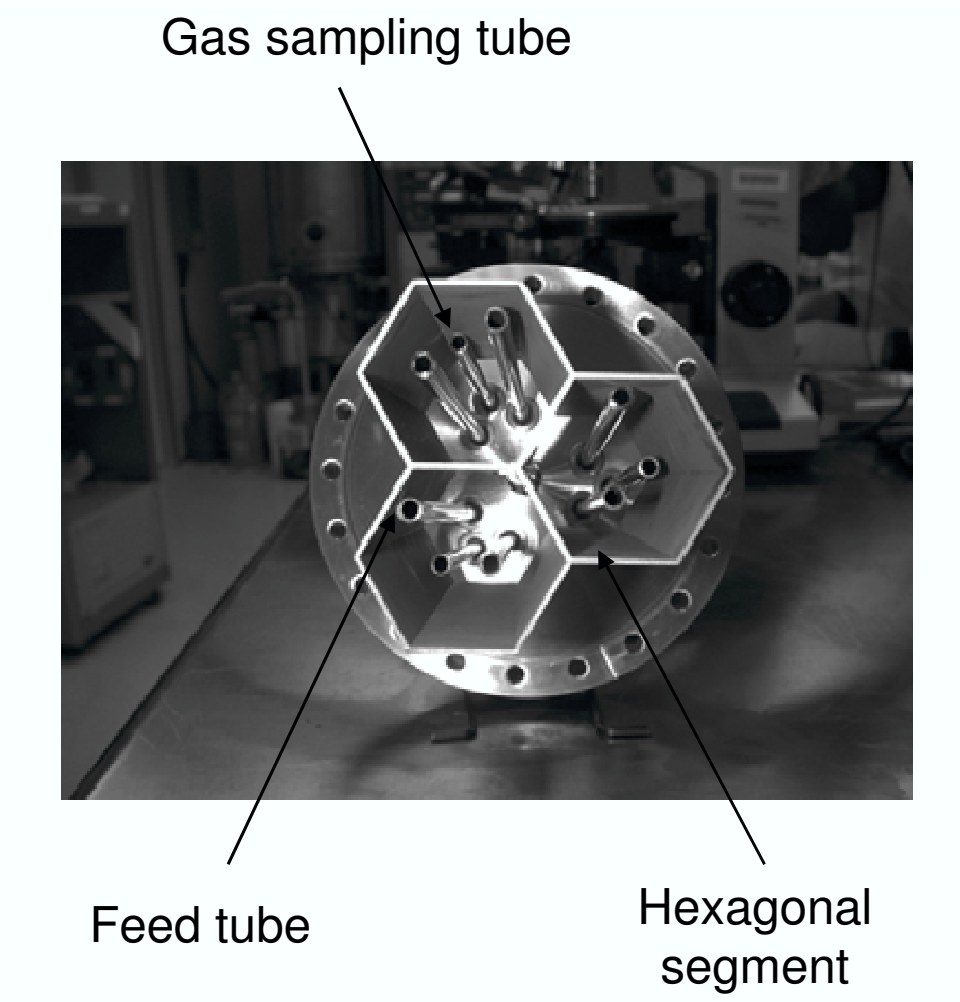

Figure 2.1: The photo image of hexagonal segment block, and feed and sampling tubes.

replaced by the new Programmable Reactor showerhead assembly. The photo image of this hexagonal segmented block is shown in Figure 2.1. The primary component of the assembly is the honeycomb-shaped array of three segments machined from a single block of stainless steel. Each side of the hexagonal segments is $W = 25.4mm$ in length and the overall length of the honeycomb segment structure is $L = 144.08mm$. As designed, the three segments cover most of the surface area of the $100mm$ wafers used in deposition experiments. The segment length was made as long as physically possible subject to the constraints imposed by clearances necessary to insert the wafer and to prevent obstruction of the exhaust ports in the showerhead chamber.

Each segment is fitted with two $6.35mm$ ID feed tubes and one sampling tube (Figure 1.1). The feed and sampling tube vertical positions can be adjusted when the reactor is not operating. The sampling tube of each segment can be used to transport a small amount of gas to a real time in-situ sensor, such as a mass spectrometer. From the residual gas analysis of each segment, approximate film thickness and the composition of film deposited on each area corresponding to each segment can be determined [25].

Individual mass flow controllers with a range of $0 - 100sccm$ were used to control the total flow of H_2, Ar, and WF_6 to the showerhead; a network of needle valves was used to split these gas flows to each showerhead segment. Showerhead/wafer spacing is controlled with the linear motion device shown in Figure 1.1. In addition to controlling inter-segment region diffusion, the linear motion device is needed to raise the honeycomb structure sufficiently to allow the cluster tool's robot arm to insert and withdraw the wafer from the reactor chamber.

2.2 Modeling and Simulation

Because of the Programmable CVD reactor's reverse-flow design, reactants in the gas mixture in the common exhaust volume can diffuse back into the segments. Therefore, to sustain the pre-specified gas compositions at the bottom of each segment, the back diffusion through the segments should be suppressed below an acceptable level by the convective upward flux contribution to species transport in each segment. A steady-state 1-dimensional segment model (for each segment) combined with a well-mixed common exhaust volume model and a model of inter-segment transport in the gap region between the wafer and showerhead segments for nonzero gap size is developed in this section. The geometry of a single segment, together with the notation used in the model development, is shown in Figure 1.1.

This model was used to determine feed gas flows to the individual segments and to interpret preliminary experimental observations. In particular, the simulator was used to assess the ability of the segmented structure to maintain significant segment-to-segment gas composition differences near the wafer surface when the reactor was operated under the extreme condition of supplying pure Ar to segment 1, pure WF_6 to segment 2, and pure H_2 to segment 3.

2.2.1 Exhaust volume

As the first step in developing a model of reactant transport through each segment (Figure 1.1) and between each segment in the wafer/showerhead gap region, the

mole fraction of each species denoted as

$$x_i^k(z) \quad : \quad i = \mathrm{H_2},\ \mathrm{WF_6},\ \mathrm{Ar} \quad \mathrm{k{=}1{,}2{,}3} \quad 0 \le z \le L$$

where the the subscript i refers to the gas species and k the segment number.

For this simulation study, the common exhaust volume was treated as perfectly mixed. Because of the relatively low depletion rate of the deposition reaction under the chosen operating conditions (this assumption will be validated at the end of this chapter), the exhaust volume composition x_i^{exh} was computed simply as the average of the feed compositions to each segment.

2.2.2 Inter-segment diffusion

The rate of across-wafer chemical species transport is determined by the gap size h between the honeycomb showerhead structure and wafer surface and the composition differences between the reactant gases at the bottom of each segment and the chamber itself. A simplified model of inter-segment transport in this gap region can be derived for the experiment where pure gases are fed to each segment. For example, the flux of Ar from segment region 1 (where it is the primary feed gas) to segment 3 (where H_2 is the primary feed) can be written as

$$N_{Ar}^{1-3} = CD_{Ar,H_2} f_d \frac{x_{Ar}^3(0) - x_{Ar}^1(0)}{2W\cos(\pi/6)} \tag{2.1}$$

where the length scale of the finite-difference approximation to the composition gradient is the distance from the center of one hexagonal segment to the center of the adjacent segment. The flux correction factor f_d will be estimated from experimental

data later in this chapter. Because the chamber gas phase composition could not be measured in the experiments discussed in this chapter and because of the likelihood of WF_6 depletion due to heated reactor components, transport between segment regions and the outer chamber are not included in this simulation study. The binary diffusion coefficients D_{ij} are estimated by the Chapman-Enskog kinetic theory and Neufield method [24] [26] C is the total gas concentration. A complete summary of the parameters and variables used is presented in Table C.1 at the end of this thesis.

These values of inter-segment species flux then are used as the initial value of the intra-segment flux terms:

$$N_i^k(z) = \frac{hW}{A_s} \sum_{n=1}^{3} N_i^{k-n} + F_i^k(z)$$

where F_i^k is a function accounting for the change in flux due to fresh feed of species i from the segment feed tubes and is defined by

$$F_i^k = 0 \qquad z < z_f$$

$$F_i^k = Q_i^k \rho_i / (M_i(A_s - A_f)) \qquad z \geq z_f$$

where Q_i^k is the volumetric flowrate of gas species i to segment k.

2.2.3 Intra-segment transport

Neglecting any effect of pressure and forced diffusion, the multicomponent gas species transport can be expressed by the Maxwell-Stefan equation

$$\nabla x_i^k = \sum_{j=1}^{n} \frac{1}{CD_{ij}} \left(x_i^k N_j^k - x_j^k N_i^k \right) + \sum_{j=1}^{n} \frac{x_i^k x_j^k}{D_{ij}} \left(\frac{D_j^T}{\rho_j} - \frac{D_i^T}{\rho_i} \right) \nabla \ln T \qquad 0 < z < L$$

subject to boundary conditions

$$x_i^k(L) = x_i^{exh}. \tag{2.2}$$

The gas temperature profile along the segment length z is needed to compute the contribution of thermal diffusion; observation of the W film deposited on the segment structure after a number of experimental runs indicates that there is significant gas and segment heating along the bottom-most third of the honeycomb segments. Given this observation, and the difficulty of obtaining accurate gas temperature measurements at low pressure, the gas temperature was approximated as a linear interpolation between the wafer (maintained at 350^{o}C) and the ambient temperature (30^{o}C) over the bottom third of the segment, and was set as the ambient temperature for the remainder of the segment.

The flux due to ordinary diffusion can be defined as

$$\bar{N}_i^k = N_i^k + \frac{D_i^T}{M_i} \nabla \ln T$$

giving the simplified form of the Maxwell-Stefan equation

$$\nabla x_i^k = \sum_{j=1}^{n} \frac{1}{CD_{ij}} \left(x_i^k \bar{N}_j^k - x_j^k \bar{N}_i^k \right) \tag{2.3}$$

subject to boundary conditions (2.2). The D_i^T are the multicomponent thermal diffusion coefficients computed using the correlations given in [24].

2.3 Simulation Results

The nine inter-segment flux equations (2.1) are solved simultaneously with the nine collocation-discretized Maxwell-Stefan equations (2.3) subject to boundary condi-

tions (2.2) using a Newton-Raphson method to obtain the gas composition profiles as a function of position within each segment. 20 collocation points located at the zeros of 19th-degree Chebyshev polynomial, plus the interval endpoints, were used to define the discretization arrays [27].

Because the modeling equations for each segment are identical in structure and vary only in terms of parameter values, an object-oriented approach was taken to setting up the simulator: a segment model class (in MATLAB) was derived from an abstract class defining the general structure of a nonlinear algebraic equation model. Methods for the nonlinear equation model class included a Newton-Raphson based equation solver, which is inherited by the segment model class. Because each segment model is an instance of the latter class, this approach is an efficient method for setting up models of this form, and is readily extensible to Programmable Reactor models with many more segment elements. More details on the computational approach are in [28].

Representative results of this solution procedure are shown in Figure 2.2. In this Figure, the wafer surface is located at $z = 0$ (the left axis limit) and the segment top is to the right; the vertical line represents the location z_f of the bottom of the feed tube bundle inside each segment. Two sets of simulations were performed to assess the effect total gas flow to each segment has on the composition profiles, and the results are discussed below. In each case, the gap size h was set to 0. Simulations to evaluate the effect of gap size h will be performed later in this chapter to interpret some of the experimental findings.

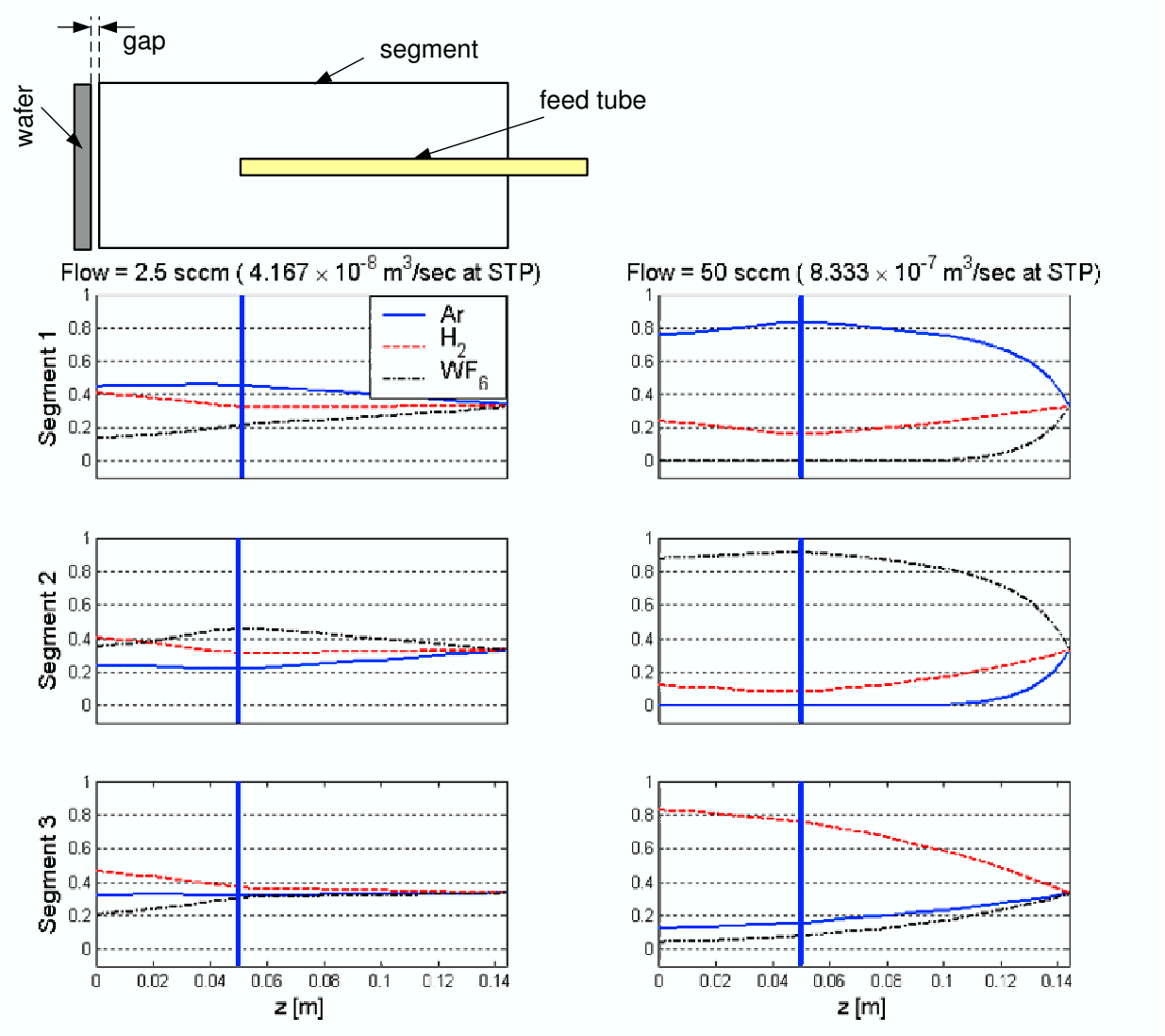

Figure 2.2: Gas composition profiles in each segment for two different gas flow rates for the Ar fed segment (top), WF_6 fed segment (middle), and H_2 fed segment (bottom); the vertical line marks the feed tube bundle outlet location.

2.3.1 Low-flow results

Simulator predictions for the gas composition profiles of Segments 1 to 3 (ordered from the top plot) for a gas feed flow of $Q = 2.5sccm$ to each segment are shown in the left column of plots in Figure 2.2. The composition in each segment as $z \rightarrow L$ approaches the composition of the gas in the common, well-mixed exhaust chamber. As the profiles are followed down the segments, the feed gas species of each segment becomes the primary component. However, because of the relatively low flow, significant back-diffusion of the other components occurs resulting in a significant fraction of each species being found near the bottom of each segment - this is particularly true in Segment 3 because of the larger fraction of H_2 and the larger values of binary diffusion coefficients when H_2 is one of the species. It is also interesting to observe the effect thermal diffusion has in this simulation - in each case, the region near the wafer is enriched in H_2 relative to the heavier species due to thermal diffusion. Thus, because of the large negative effect ordinary and thermal diffusion have on the ability to control gas composition near the wafer surface, it is possible to conclude that higher feed flow rates should be used.

2.3.2 High-flow results

Increasing the gas flowrate to $50sccm$ in each segment has a dramatic effect on the gas composition profiles in each segment. As can be seen in the right column plots of Figure 2.2, the feed species to each segment becomes the dominant gas phase species near the wafer surface. Thermal diffusion effects still can be observed, but have a

much lower impact on the composition profiles. Under these operating conditions, the effect of changing the gap size on gas composition near the wafer surface should be more pronounced, and so initial experiments were conducted at these conditions. It should be noted that the while the WF_6 concentration at the bottom of Segments 1 and 3 is very small, it is nontrivial and so can (and does) result in film deposition under these segments.

2.4 **Prototype Experimental Tests**

Initial experiments were performed using the three zone prototype to validate two basic Programmable Reactor design concepts: (1) that the reverse-flow showerhead design could maintain significant segment-to-segment gas-phase compositional differences near the wafer surface, and (2) that spatially patterned wafers could be produced by this reactor design and that some of the characteristics of the pattern can be controlled by manipulating the showerhead/wafer gap. Typical operating conditions for the first experiments consisted of a 66.662 Pa chamber pressure, a wafer temperature of 350^{o}C, and 10-20 minute deposition times. The film thickness in the region below each segment was determined by sheet resistance measurements using a four-point probe.

2.4.1 Segment-to-segment gas composition differences

In one set of representative experiments, pure Ar was fed to Segment 1 at a flowrate of $50 sccm$; $50 sccm$ of WF_6 was fed to segment 2, and $50 sccm$ of H_2 was fed to segment 3. Sheet resistance measurements were made at seven points on the wafer

surface in each segment region; the location of the data points are shown in Figure 2.3. Simulator predictions for these conditions indicate that the gas composition at the wafer surface is mainly the segment feed species, with a small amount of WF_6 present at the bottom of segments even when $h = 0$ (Figure 2.2). While W deposition should take place directly under Segment 2 (where pure WF_6 is fed) due to the Si reduction mechanism, it is interesting to note that some W deposition takes place under the remaining two segments. Experimental data and simulator predictions in the remainder of this chapter will validate that the WF_6 responsible for deposition in segments 1 and 3 is transported to this region through a combination in back-diffusion and inter-segment diffusion.

2.4.2 Control of pattern resolution

In all cases where the showerhead/wafer spacing was small (e.g., $h = 1mm$), distinct hexagonal film patterns were produced (Figure 2.4). As the gap is increased, the contribution of back-diffusion down the segments from the common exhaust remains essentially constant while inter-segment diffusion in the gap region increases. Photographs of wafers processed for three different gap values are shown in Figure 2.4 demonstrating that the pattern becomes more diffused with increasing gap size. This decrease in the sharpness of the deposition pattern provides visual evidence for the effectiveness of using gap size to control inter-segment diffusion of reactant species across the wafer surface.

Across-wafer diffusion of WF_6 from Segment 2 to the Ar- and H_2-fed segments should result in a negative film thickness gradient along lines drawn through the

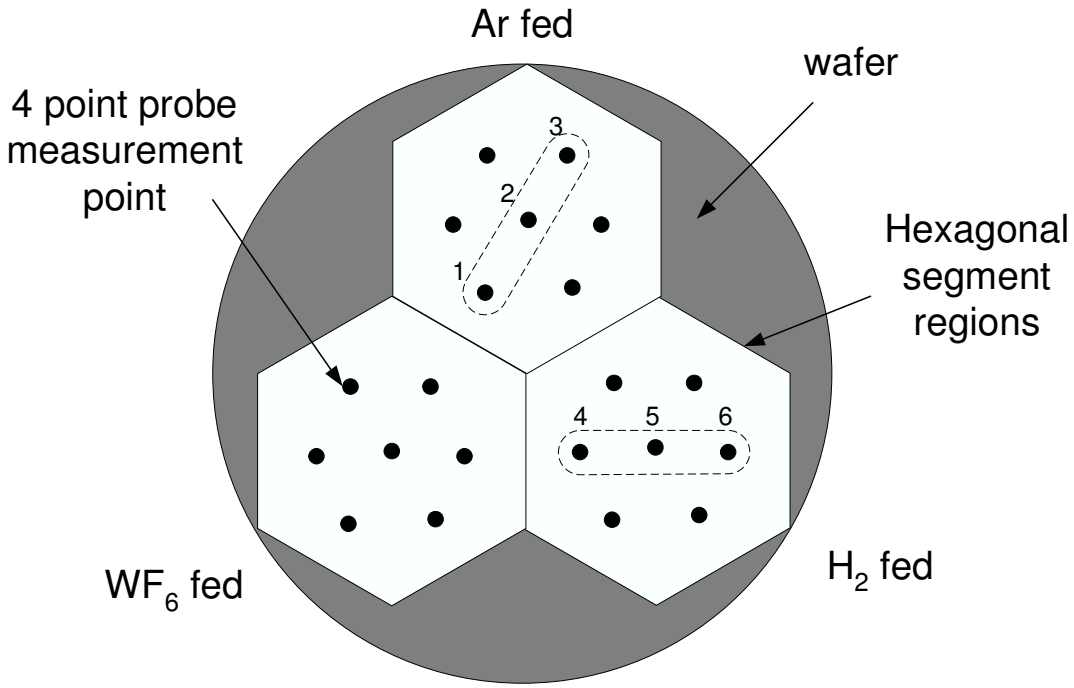

Figure 2.3: Film thickness measurements point locations (determined by sheet resistance measurements) relative to segment locations; seven measurements were made in each segment region.

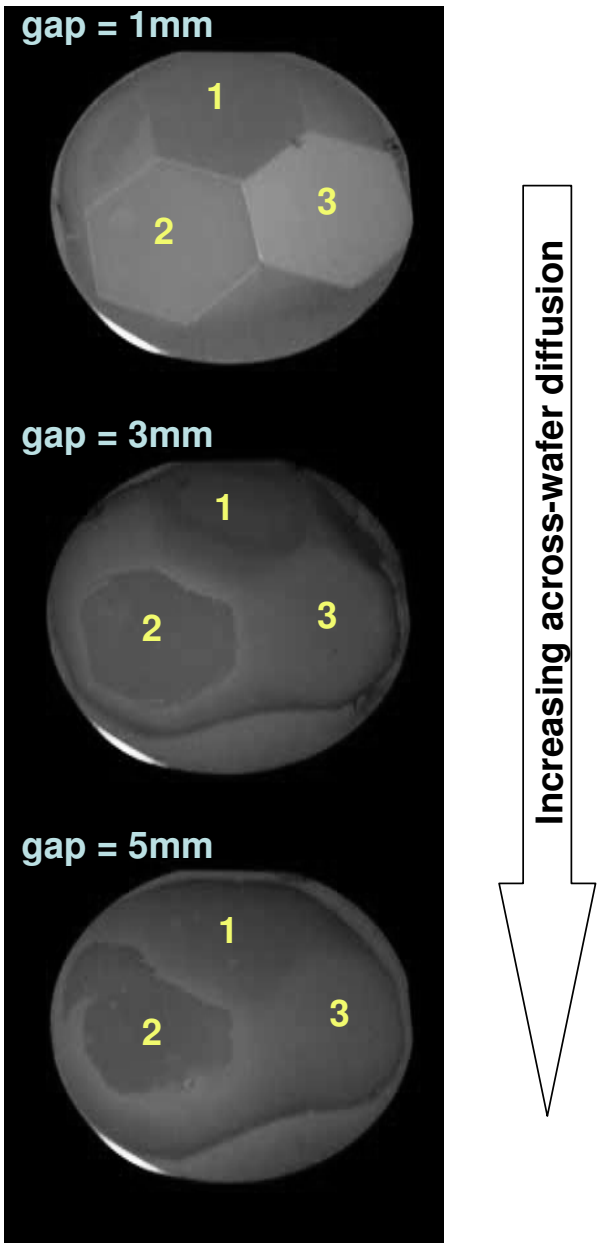

Figure 2.4: Deposition patterns produced using three different values for the showerhead/wafer gap spacing. In these experiments, pure Ar, WF_6, and H_2 were fed to the individual segments.

latter two segments in the direction away from Segment 2 (as seen in the two sets of measuring points; 1, 2 and 3 for Ar fed segment, and 4, 5 and 6 in H_2 fed segment in Figure 2.3). This is clearly evident in the linear interpolation plots presented in Figure 2.5, where the film thickness along these two "cuts" in Segments 1 and 3 is plotted for three different values of gap size. Furthermore, one can observe the overall thickening of the film in these two segments as the gap increases, a phenomenon attributable to the increased WF_6 concentration resulting from increasing inter-segment diffusion as the gap is increased. Likewise, extrapolating the growth rates of Segments 1 and 3 to $h = 0$ (which is an undesirable experiment to perform) shows positive growth rates in each segment for zero gap, indicating the contribution of intra-segment back-diffusion of WF_6 to the growth rate in each of these segments. It is interesting to note the greater slope of the deposition rate line in Segment 1 relative to Segment 3; this may be attributable to the smaller binary diffusion coefficient in an Ar-WF_6 mixture compared to a H_2-WF_6 mixture.

Finally, error bars indicating the standard deviation of all seven sheet resistance measurements per segment are plotted; the slightly increasing trend with gap size may indicate additional effects of inter-segment and chamber-segment diffusion on film thickness variation within each segment region as the gap increases. For increasing values of very large values of h (e.g., $< 10mm$), the variability should begin to decrease with h due to the dominance of across-wafer diffusion under these operating conditions.

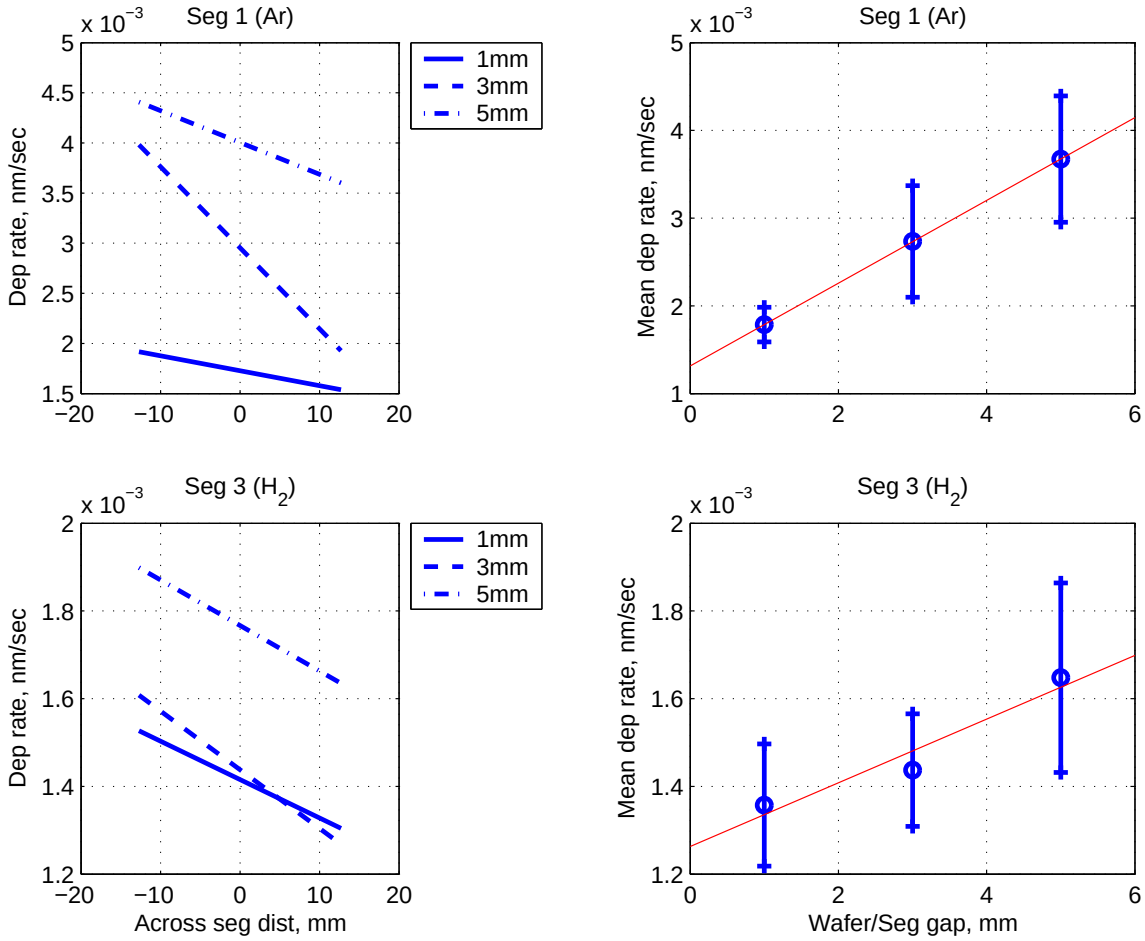

Figure 2.5: Film thickness measurements for three showerhead/wafer spacing values showing how film thickness decreases in the Ar and H_2 fed segments with distance from the WF_6 segment (left) and how overall film thickness increases in each segment region as the spacing is increased (right)

2.5 Simulation-Based Interpretation of Film Deposition Results

Thin films of tungsten can be deposited in either a selective or blanket tungsten deposition mode. The gas phase reactions associated with these deposition processes are negligible due to low reactor pressure during the process operation [21] [23], therefore, the deposition rate is determined only by surface reaction and chemical species transport rates in the gas/wafer surface interface and through the deposited film itself.

The overall reaction of tungsten deposition by hydrogen reduction on a silicon wafer substrate begins with surface reactions by Si reduction during the film nucleation step; the reaction is

$$2\ WF_6(g) + 3Si(s) \longrightarrow 2W(s) + 3SiF_4(g)$$

in the range of deposition temperature used in our experiments [29]. Numerous studies have focused on the extent to which this reaction takes place and when the transition to the H_2 reduction process

$$WF_6(g) + 3H_2(s) \longrightarrow W(s) + 6HF(g)$$

occurs (see Appendix A for more information on W film growth kinetics). Most studies conclude the Si reduction step is self limiting and typically accounts for 10-200nm of W film thickness at the Si substrate/W film interface [30]. However, Joshi, Prasad, Yu and Scilla presented a counterexample study in which non-self-limited growth was observed using two different CVD systems, resulting in relatively thick W films [31]. A mechanism for this deposition process was proposed whereby Si out-diffused from the substrate through the deposited W film and reacted with WF_6 on

the film surface; this process was found to be promoted by oxygen impurities in the W film. The expression for the overall deposition rate was determined to depend on the product of the film surface Si concentration and the gas WF_6 concentration at the film surface:

$$N_{Si}\frac{ds_w}{dt} = R_k C_i$$

(after eq. A5 [31]) where N_{Si} is the number density associated with the growing film scaled by the number of Si moles required to produce 1 mole of W film, and s_w is the film thickness. The first term in this product is attributable to the surface reaction which is n-th order in WF_6:

$$R_k = K_0 e^{-E_a/RT}[Cx_{WF_6}]^n. \tag{2.4}$$

The second term is derived from the assumption that Si transport through the W film is governed by Fick's Law; a finite difference approximation to the diffusion flux together with the assumption that the diffusive flux is in equilibrium with the surface reaction above gives the term associated with the surface Si concentration as:

$$C_i = \frac{C_0}{1 + K_0 s_w [Cx_{WF_6}]^n e^{-E_a/RT}/D}.$$

where C_0 is the concentration of Si in the W film at the W/Si interface and D is the diffusion coefficient of Si in W. See [31] for a more detailed derivation of these rate expressions. For short deposition times or thin films ($s_w \to 0$) produced by low deposition temperature or low WF_6 concentration, $C_i \to C_0$ and the deposition rate is determined only by the surface reaction rate R_k (in the absence of gas-phase transport limitations), thus

$$\frac{ds_w}{dt} = \frac{C_0 K_0}{N_{Si}} e^{-E_a/RT} C^n [x_{WF_6}]^n. \tag{2.5}$$

2.5.1 Simulated vs. measured deposition rates

Simulation of the deposition process in Segments 1 and 3 can be used as an indirect method to quantify the rate of inter-segment transport in the wafer/showerhead gap region. This will be carried out by estimating the parameter f_d in (2.1) and the reaction rate coefficients $K^k(T)$ in the simplified rate expression (2.5) for growth of very thin films by Si reduction in segments $k = 1, 3$:

$$\frac{ds_w^k}{dt} = K^k \left[x_{WF_6}^k(0) \right]^n$$

where

$$K^k = \frac{C_0 K_0}{N_{Si}} e^{-E_a/RT} C^n.$$

Simulations were performed using the three-segment reactor model for gap values of $h = 1, 3, 5mm$ and a fixed value of f_d to obtain the values of $x_{WF_6}^k(0)$ for segments $k = 1, 3$. Because Si reduction depends on the surface condition of the silicon wafer, a least-squares fit of the rate coefficients K^k to the experimentally measured rate data was performed for each segment instead of using a constant value for all segments; the optimal value of f_d was determined by minimizing the error in this regression. This approach is not inconsistent with Joshi, Prasad, Yu and Scilla [31], where parameter fitting was used to determine the reaction rate pre-exponential constant K_0 and the activation energy E_A. The parameter values

obtained using this estimation method are:

$$f_d = 0.2 \qquad K^1 = 1.92\,nm/min \qquad K^3 = 0.36\,nm/min$$

Simulator predictions of growth rates as a function of h are compared to experimental data in Figure 2.6.

That a good fit is obtained for the rate exponent of $n = 0.5$ (recommended by Joshi, Prasad, Yu and Scilla [31]) is significant because an accurate rate description for rates linear in WF_6 concentration and that pass through $ds_w/dt = 0$ for $x_{WF_6} = 0$ could not be found for these data. The different values of K^k determined for each segment can be attributed to the different wafer surface temperatures in each segment due to gas composition differences [32] or film surface condition differences resulting from the H_2/Ar composition differences.

The resulting simulator predictions are consistent, qualitatively as well as quantitatively, with the observed reactor behavior, indicating the importance of intra-segment back-diffusion and inter-segment diffusion across the wafer surface in governing the observed deposition rates, and how these processes can be controlled by adjusting the gap size and feed gas flow rate in this reactor design. Finally, in Table 2.1, the magnitude of gas species fluxes due to bulk flow up the segment, the (gas phase) diffusion processes, and the deposition rate are compared to justify the original assumption that the deposition rate is low compared to the transport processes and could be neglected in the original derivation of the reactor segment model.

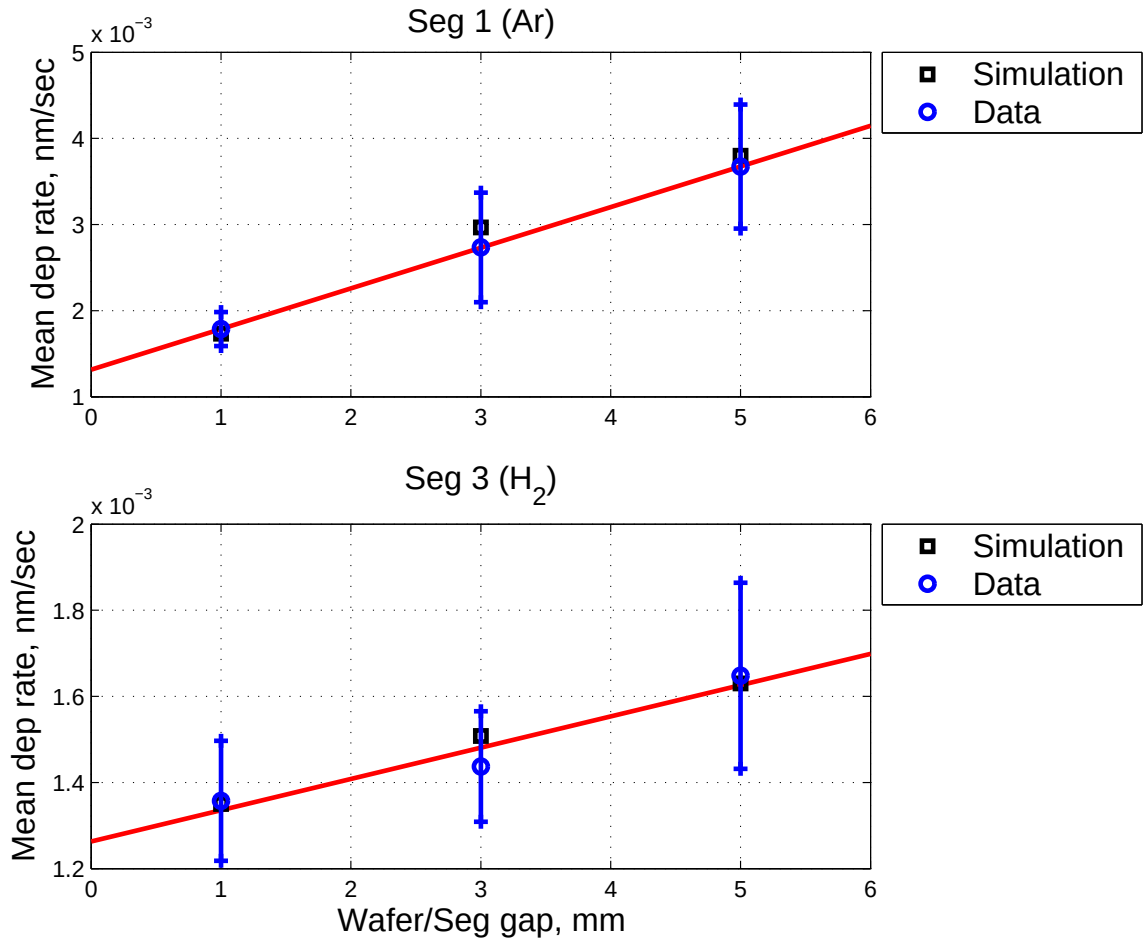

Figure 2.6: Simulated predictions of the W deposition rate by Si reduction in the Ar and H_2 fed segments compared to experimental measurements.

Flux	*Value, mol/(m^{2}s)*
convective (F_i^k)	O(10^{-2})
intra- and inter-segment (N_i^{j-k})	O(10^{-5})
deposition rate	O(10^{-7})

Table 2.1: A comparison of fluxes predicted by the reactor simulator.

2.6 Chapter Summary

A new approach to designing spatially controllable chemical vapor deposition reactors was presented in this chapter. The primary design innovation of this CVD system was the introduction of a segmented, reverse-flow gas delivery (showerhead) assembly. A three segment prototype reactor was constructed to prove the validity of the design concept and provide engineering data for simulator development. Preliminary experimental testing demonstrated the validity of the design by depositing spatially patterned films using the reactor's ability to control across wafer gas composition. Simulation studies were performed to interpret experimental data and to estimate gas phase composition at the wafer surface.

This approach to thin-film manufacturing control opens the door to a new generation of CVD reactor designs, allowing single-wafer combinatorial studies and precise across-wafer uniformity control in a single reactor design. The modular nature of the showerhead segments offers the possibility of developing CVD reactors for very large substrates. To reach these goals, a new reactor was constructed that includes a more precisely controllable reactant gas delivery system, a cleaner reaction chamber environment, and better access to the wafer while the deposition process is taking place. Details regards construction of testing the second prototype will be discussed in the next chapter; the additional instrumentation in the next prototype will allow a demonstration of the programmability capabilities envisioned for this system.

Chapter 3

Construction of Prototype System P2 and Evaluation of its Combinatorial Processing Capabilities

Rigorous simulation and a sequence of experiments performed on a prototype reactor to prove the feasibility of the spatially controllable CVD reactor concept were discussed in chapters 1 and 2. This first prototype reactor (P1) consisted of a modified commercial Ulvac ERA-1000 CVD cluster tool. Preliminary simulations and experiments with this modified reactor system were used to quantify segment back diffusion and inter-segment diffusion contributions to film growth, and to demonstrate intentional spatially non-uniform film deposition.

While preliminary experiments with prototype P1 successfully demonstrated the feasibility of this new approach to controllable CVD, the experiments uncovered limitations in the prototype system. For example, in the first prototype, only one feed line of each segment was connected to a mass flow controller, limiting the range of process recipes that could be tested. As a result, this feed gas supply configuration did not allow W deposition by H_2 reduction and prevented a true test of programmability. Also, the first prototype system could only reach 10^{-4} torr as a base pressure because the original Ulvac system was designed for low pressure chemical vapor deposition (LPCVD). This relatively high base pressure caused several contamination problems including particle generation, high partial pressures of H_2O, CO_2, and O_2 in gas phase, and unusual deposition patterns. The reactor system also required a significant amount of conditioning time to lower the partial pressure of undesirable gas species, such as H_2O, CO_2, and O_2 that would

consume the reactive WF_6 during processing. The non-flexible design of the original Ulvac system also was a serious limitation of first prototype system in terms of lack of ability to add new sensors and gas lines, and to repair chamber components, such as the segmented showerhead assembly and substrate heater. To overcome this limitation and demonstrate the true capability of spatially controllable reactor system, new prototype reactor was needed. This new flexible reactor system is highly flexible enough in changing process condition to be capable for CVD combinatorial research as library wafer producing tool.

In this chapter, the design and construction of a new prototype reactor with combinatorial capabilities will be discussed as well as the experimental results demonstrating W CVD by H_2 reduction performed with this reactor. In the chapter summary section, future research for improving the performance of this reactor system is discussed.

3.1 Combinatorial CVD

Most film deposition in combinatorial research is performed in physical vapor deposition process because the ability to control gas transport to directly affect film composition is limited in conventional CVD reactor systems. Limited success in developing CVD systems for combinatorial research has been reported [33] [34].

Because the Programmable CVD reactor system was designed to have significantly greater sensing and actuation capabilities relative to conventional CVD reactor designs, the Programmable Reactor takes its name from the ability to rapidly alter reactor geometrical characteristics as well as the reactant gas conditions, all in

software. With its fast reprogramming capabilities, this new CVD reactor design is an ideal tool for combinatorial materials development research because of its ability to produce films with properties that change (smoothly or sharply) across the wafer by varying the operational parameters of the system, which include wafer/segment gap size, gas flow rates, and the gas composition in each segment [35]. In Figure 1.2 a rapid process prototyping approach to new materials and process development was illustrated. Carrying out the processing concept shown in Figure 1.2 requires an accurate simulator to extrapolate the measurements available from the segment sampling to the wafer surface.

3.2 The Prototype P2 Reactor System

To demonstrate the true performance capability of this spatially controllable CVD system effectively, it was necessary to construct more flexible prototype CVD system that could be operated as a clean ultra high vacuum (UHV) capable system (see Figure 3.1, Figure 3.2 and Figure 3.4). The prototype reactor system P2 consists of four major components: the 1) loadlock and reaction chambers, 2) gas distribution box, 3) two sets of exhaust gas pump systems, and 4) a gas composition sensing system consisting a mass spectrometer and sampling lines. The process equipment layout is shown in Figure 3.3. The differences of prototype system P1 and P2 are briefly described in Table 3.1.

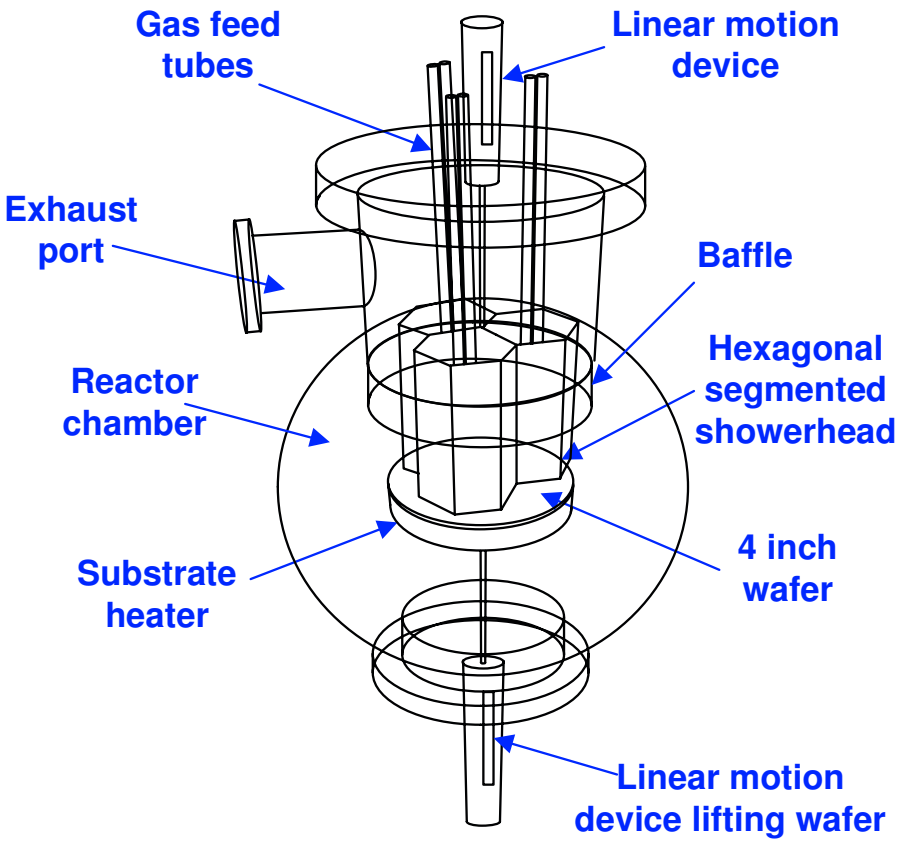

Figure 3.1: Diagram of the prototype P2 reactor chamber, hexagonal showerhead, heater, and feed and sampling tubes.

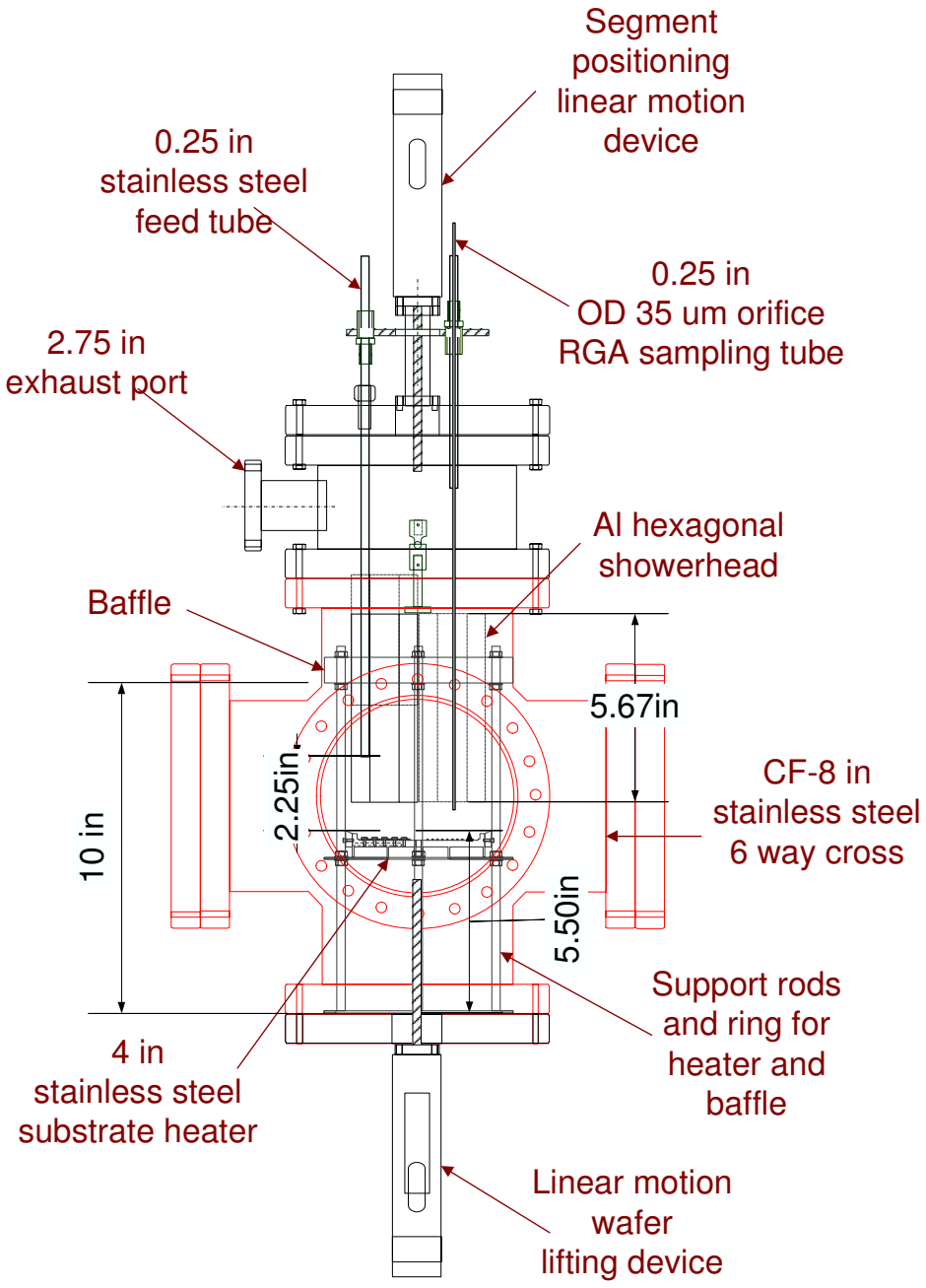

Figure 3.2: Detailed mechanical drawing of the new reactor chamber, showerhead and heater with critical dimensions such as wafer to feed tube distance, segment length, and heater and baffle positions.

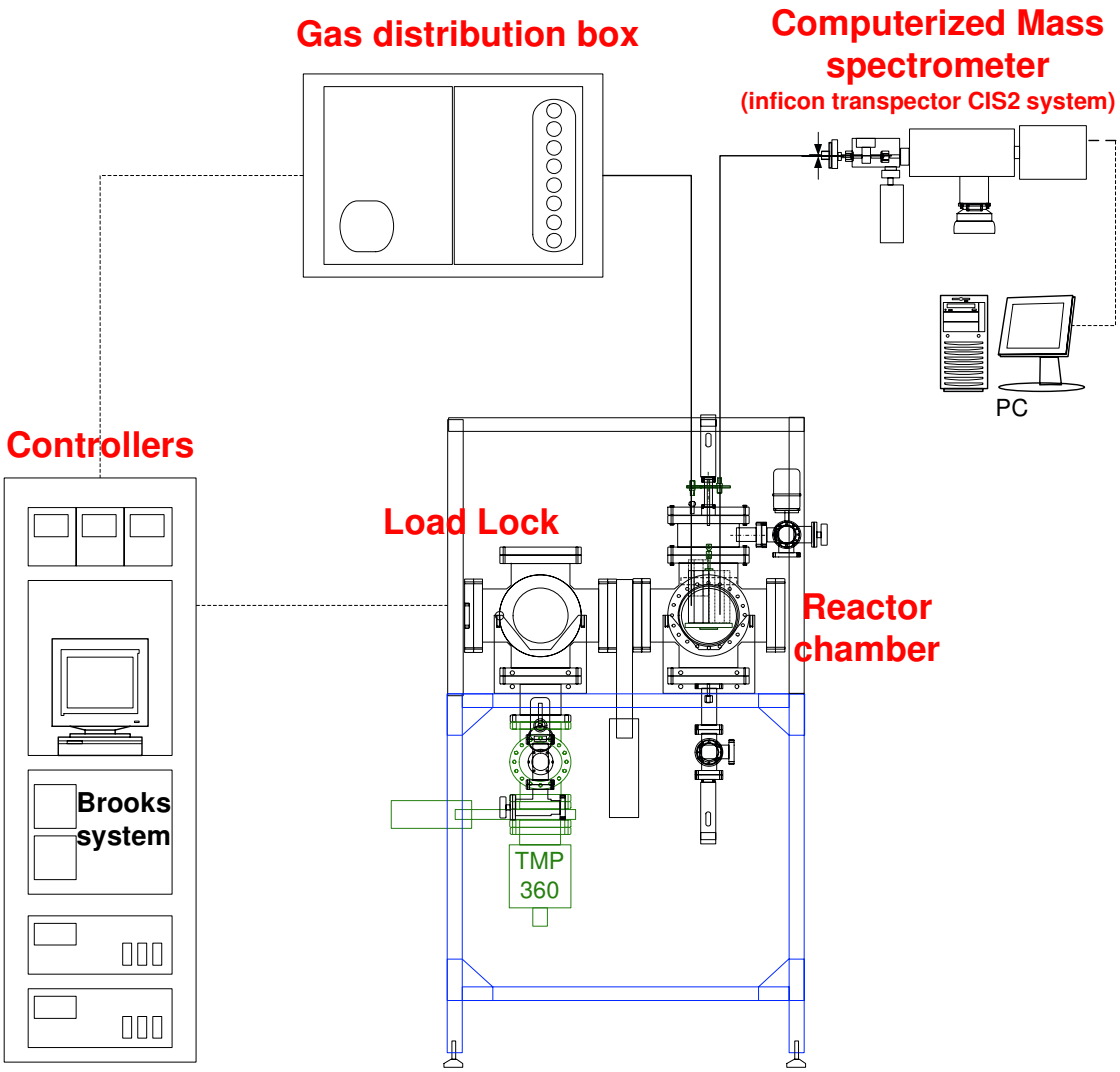

Figure 3.3: Overall configuration of the Prototype 2 system.

Prototype system	P1	P2
Reaction chamber base Pressure [torr]	10^{-4}	$< 10^{-8}$
Loadlock chamber base Pressure [torr]	10^{-3}	$< 10^{-8}$
Pressure gauges on reaction chamber	1 [b] and 1 [c]	1 [b], 1 [c] and 1 [i]
Pressure gauges on loadlock chamber	1 [c]	1 [c] and 1 [i]
Feed tubes per segment	1	3
Gas sampling capability	No	Yes
Gas source monitoring capability	No	Yes
Chamber baking capability	No	Yes
Process control	semi-automatic	automatic

Table 3.1: Differences of prototype system P1 and P2 ([b]-Baratron type pressure gauge, [c]-Convectron type pressure gauge, [i]-ion gauge).

3.2.1 Chambers and pumps systems

Two standard stainless-steel 8 inch 6-way CF crosses are used for the loadlock and reaction chambers. The diagrams and detailed mechanical drawing of the new reactor chamber with programmable showerhead and heater are shown in 3.1 and 3.2. The loadlock chamber is used to minimize air exposure to the reactor chamber and is pumped with one set of turbo-molecular and mechanical pumps resulting in a loadlock chamber base pressure of 10^{-8} torr. This UHV condition was achieved after He leak checking using the mass spectrometer on this system, normally used for residual gas analysis (RGA). The reaction chamber is pumped by a similar arrangement resulting in a base pressure lower than 10^{-8} torr. Because of these low base pressures, the contamination sources from chamber wall are eliminated. The chamber and pump diagram is shown in Figure 3.4, along with the gas distribution box and mass-spectrometer sampling system.

As shown in Figure 3.4, the reaction chamber is isolated by two gate valves, minimizing the air exposure when pumps or gauges are repaired. During a CVD process, residual gas is pumped through the top of each segment into the common exhaust volume and then through valve (2) to the 4-way cross. This 4-way cross allows the gas pumped through the turbo-molecular pump and valve (3) flow to the mechanical pump. During chamber cleaning, gas evolving from chamber walls is pumped through valve (1) and the 6 inch 4-way cross, then is exhausted to the turbo-molecular pump and backing mechanical pump.

Each chamber has a set of pressure gauges consisting of an ion gauge measuring

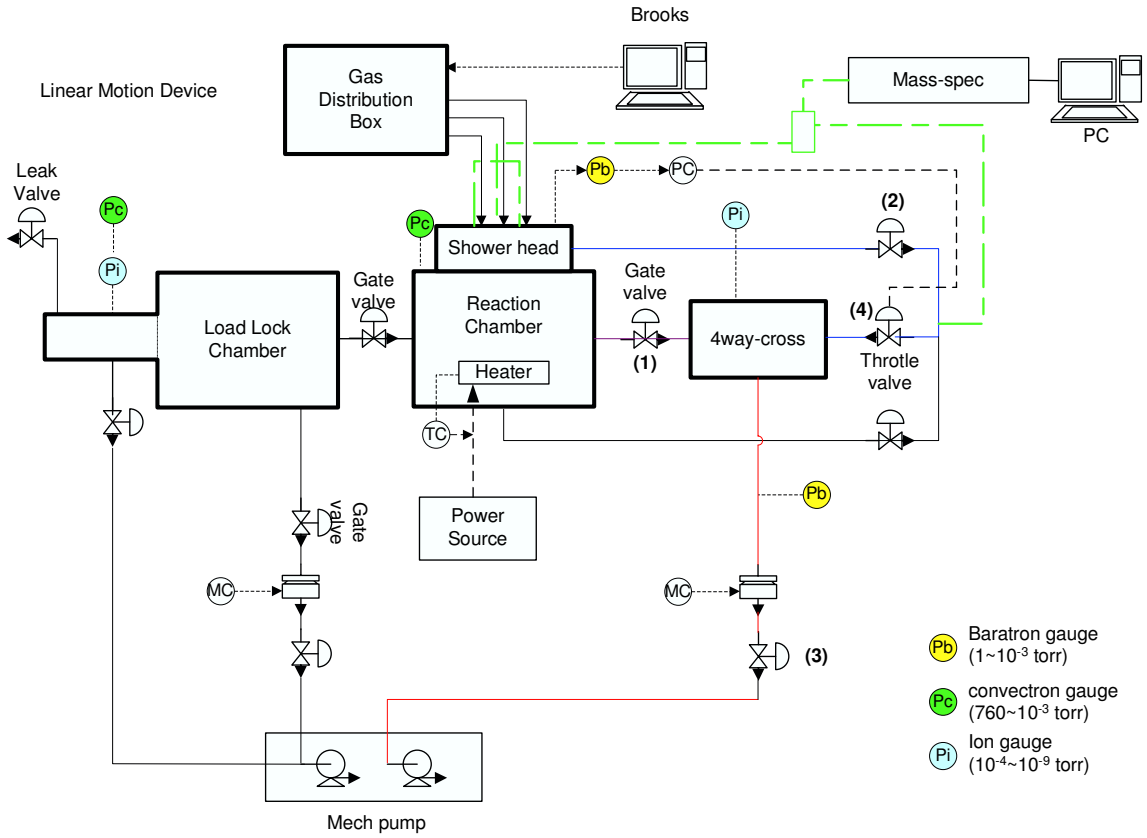

Figure 3.4: The diagram of the Prototype 2 system (gas flow control system, pumps, chambers, gas distribution box, mass-spectrometer, and controllers).

chamber pressure from 10^{-8} to 10^{-4} torr and a convectron gauge for the 10^{-3} torr to atmospheric pressure range. These ion and convectron gauges are easily damaged by corrosive gases such as WF_6. A Baratron diaphragm type gauge is used for pressure control sensor in the reaction chamber with throttle valve (4).

Gas sampling lines are built into the gas exhaust line to facilitate mass-spectrometer based leak checking, a necessary procedure to maintain a UHV chamber. During the process, a 50 micron orifice is inserted into the sampling tube to reduce the process pressure down to the required mass-spectrometer pressure. However, during cleaning, the 0.25 inch (OD) standard stainless tube is used directly. The sampling lines and mass-spectrometer are shown in Figure 3.4. This mass-spectrometer also will be used for segment-to-segment multiplexed process monitoring through the individual gas sampling tubes in each segment.

3.2.2 Gas distribution box

To control gas flow rate and composition to each segment, a gas distribution system was developed to provide control to 9 sets of gas feed lines; 3 gas lines distribute gas to each segment and each is connected to a Ar, H_2 and WF_6 gas source. A gas line assembly consists a mass flow controller (MFC), one manual and two pneumatic valves, a pressure gauge, and a pressure regulator. A schematic diagram of the gas distribution box and gas delivery lines are shown in Figure 3.5

The setpoints of the pneumatic valves and mass flow controllers are sent from a Brooks automation system master controller. The one set of pneumatic on/off valves is installed in each gas line near to the reactor, instead of in the gas distribution

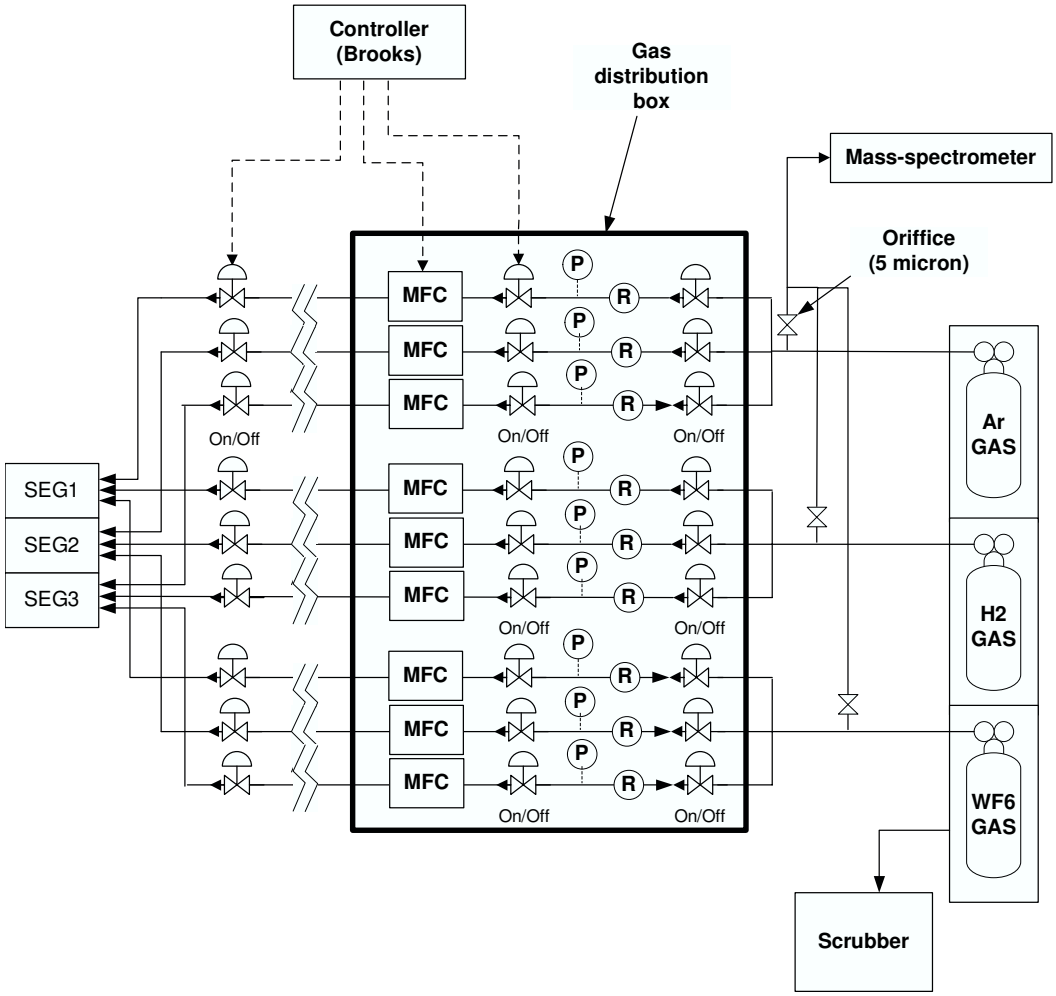

Figure 3.5: Schematic diagram of the gas distribution box and its components.

box, to minimize exposing gas feed lines to air during maintenance.

If air or water vapor are introduced to the WF_6 gas line, WF_6 will be consumed to produce WOF_4, HF and W particles; the corrosive HF and W particles can damage or clog on the WF_6 MFCs. To minimize contamination and achieve reproducible experimental results, gas source monitoring is necessary. An orifice in each sampling tube restricts the flow of sampled gas to protect the mass spectrometer from excessive pressure damage. For safety, the corrosive and toxic WF_6 gas source is contained in gas cabinet and is connected to a dry scrubber for venting.

3.2.3 Gas composition sensing

A novel approach to gas composition sampling also is implemented in prototype P2. Quadruple mass spectrometry (QMS) is one of the most widely used methods for in-situ real-time process monitoring. QMS instruments are compact and cost effective, as well as selective and sensitive, metrology tools [36]. Also, because the mass spectrometer can directly sense gas composition at specific point of reactor system without disturbance to process performance, it is a candidate sensor for real-time control, such as deposition time adjustment based on end-point detection during processing. Recently, mass spectrometry has been shown to be successful for end-point detection and run-to-run control [37] [38].

The sampling tube of each segment can be used to transport a small amount of gas to a QMS (an Inficon transpector CIS2 mass spectrometer is used). From the residual gas analysis of each segment, approximate film thickness and the composition of film deposited on each area corresponding to each segment can be deter-

mined. Coupled with the reactor segment model described earlier in this thesis and in [35], this capability of individual segment sampling and monitoring allows fast reprogramming of the recipe across the wafer surface using model based, real-time control or after a batch in a run-to-run control mode.

To monitor gas composition in each of the three segments pseudo-simultaneously during operation, the single mass spectrometer must have time-sharing capabilities. Three sampling tubes and on/off valves connect the segments to the mass spectrometer. The three on/off valves are sequentially opened and closed by a control signal sent from a Techware Brooks control platform to perform the mass spectrometer multiplexing. The schematic diagram of this setup is shown in Figure 3.6.

3.3 **Wafer Temperature Distribution**

Wafer temperature is the other key factor affecting film growth uniformity in most CVD processes. To reveal the heat transfer mechanisms primarily responsible for affecting wafer temperature and its uniformity, temperature measurement experiments were performed with an instrumented wafer over a range of operating conditions and reactor geometries. With a thermocouple instrumented wafer, temperatures of 13 specific points are measured. In Figure 3.7, the positions of 13 thermocouples and their relationship to the segment positions are shown.

To assess gas composition and wafer/segment gap size on wafer temperature, the wafer temperatures were measured when the chamber was filled with typical reactant gases (Ar, N2, H2) at 1 torr and a high vacuum for a range of gap sizes. Results are summarized in Figures 3.8 and 3.9, illustrating the significant effect gas

composition has on wafer temperature, and the much more minor effect gap size has on temperature in all cases except in vacuum. The role of temperature distribution in interpreting deposition results will be discussed later in this chapter.

It is believed that thermal conductivity differences between different mixture gases of each recipe may play a role in non-uniformity of wafer temperature. To assess this gas composition effect, the wafer temperatures were measured when the chamber was filled with typical reactant gases (Ar, N_2, H_2) at 1 torr and a high vacuum condition at 400^{o}C heater setpoint. To minimize the other effects such as segment position, the segment assembly was lifted up to the highest position (32 mm from wafer surface). The temperature measurement results of this experiment are shown in Figure 3.8.

As can be seen in Figure 3.8 this figure, significant temperature differences are observed for different operating conditions. Among the cases in which the chamber is filled with each gas, the largest average temperature difference was found to be approximately 20^{o}C between H_2 and Ar filled cases. The heat conduction through the gas phase between the heater surface and wafer bottom results in different average temperatures and the average temperature of the wafer increased with increasing gas heat conductivity. Thus, the H_2 filled case has the highest average temperature. However, when the reactor is filled with H_2, temperature uniformity is much worse than the other cases (Left in Figure 3.8). Considering the non-uniform temperature distribution of the heater surface, the non-uniform wafer temperature is due to the closer thermal coupling between the wafer and heater elements because of the higher thermal conductivity of H_2. The physical geometry of the reactor compo-

nents also relates to wafer temperature because radiation and heat conduction to the showerhead constitutes a major heat loss from the wafer surface.

To assess these effects, the wafer temperature measurement experiments were performed with varying wafer/segment gap size. For this second experiment, the heater temperature was set at 400 ^{o}C and the gap size was adjusted to measure wafer temperature corresponding the gap range of 5 mm to 32 mm under high vacuum conditions and at 1 torr pressure for three different gases (Ar, H_2, N_2). As shown in Figure 3.9, average wafer temperature is affected by wafer/segment gap size. Under high vacuum conditions, temperature decreases with increasing gap size and the gradient of wafer temperature is larger than the cases where the reactor is filled with gas. The reason for the decreasing temperature in the high vacuum case is that higher positions of the segment assembly allow the wafer to face an increasing area of cool reactor wall, resulting in additional wafer heat loss.

3.4 W Deposition Experiments: H_2 Reduction

The programmable CVD reactor is designed to produce intentional spatial patterns of W films on the wafer surface as well as uniform W films. In the new prototype reactor P2, H_2 reduction is performed to test this concept of spatial controllability. Intentional non-uniform deposition ability is important for demonstrating true programmability of deposition and for combinatorial materials discovery research.

3.4.1 Experiment conditions

The recipes used for the experiments are shown in Table 3.2. The recipes EXP1 and EXP2 are designed for uniform and intentional non-uniform W film deposition, respectively. In each recipe, the ratio of H_2 and WF_6 in each segment is fixed at the 4:1 ratio used for a typical blanket W deposition because the ratio of the reactant gases also affects the growth rate of W film as well as pressure, temperature and contamination on the wafer surface [39] [23] [40]. To minimize convective interaction between segments, the total flow rate to each segment was held constant set at 60 sccm for both EXP1 and EXP2.

The heater temperature was set at 400 ^{o}C and total reactor pressure was set at 1 torr, a typical LPCVD (low pressure chemical vapor deposition) condition for W deposition. According to the temperature measurement experiments, the actual wafer temperature is approximately 355^{o}C at the 400^{o}C setpoint of heater temperature.

When W deposition by H_2 reduction is performed on a Si wafer without an adhesion or barrier layer, WF_6 reacts first with Si rather than H_2. This Si reduction is sometimes self-limited (compare to the discussion in chapter 2) because Si supply from the substrate to the film's surface in contact with the reactant gas is limited by the W film growing by Si reduction. This Si reduction is not desirable for micro-electrical device fabrication because of the well-known encroachment and W migration through Si which can damage devices [41] [42] [1]. However, in this experiment, seed layer formation by Si reduction is not avoidable and is necessary

to grow W film by H_2 reduction. Considering the seed layer formation, deposition time should be sufficiently long to allow neglecting the W deposited by Si reduction. By the QMS RGA of byproduct gas SiF_4 from Si reduction, the deposition time was chosen to be 10 minutes during which Si reduction occurs for the first 10-20 seconds producing a several-nanometer thick W film.

Proper cleaning of the Si wafer surface is necessary because the W film growth is significantly affected by the surface condition of the Si wafer. For example, H_2 reduction cannot produce W films on native oxide (SiO_2), a film which usually exists on the surface of a Si wafer. Also, other organic and non-organic particles and molecules cause catalytic reactions consuming WF_6. To minimize these effects, each Si wafer (100) is cleaned with acetone and rinsed with de-ionized water to remove organic contaminants. Then, the wafer is dipped into a 10% HF solution for 5 minutes to remove native oxide and metal contamination completely.

3.4.2 Uniform deposition experiments

To establish a baseline to which intentional non-uniformity control will be compared, recipe EXP1 was fed to the segments to measure the segment-to-segment uniformity. Using the experimental conditions described in the previous section, W deposition by H_2 reduction was performed. The resistance of the W film produced in this experiment was measured to generate a 2-dimensional thickness contour map using an automatic high resolution 4 point probe which was developed for the analysis of deposition by the programmable reactor. The automatic 4 point probe station and its principle of resistance measurements are described in Appendix B.

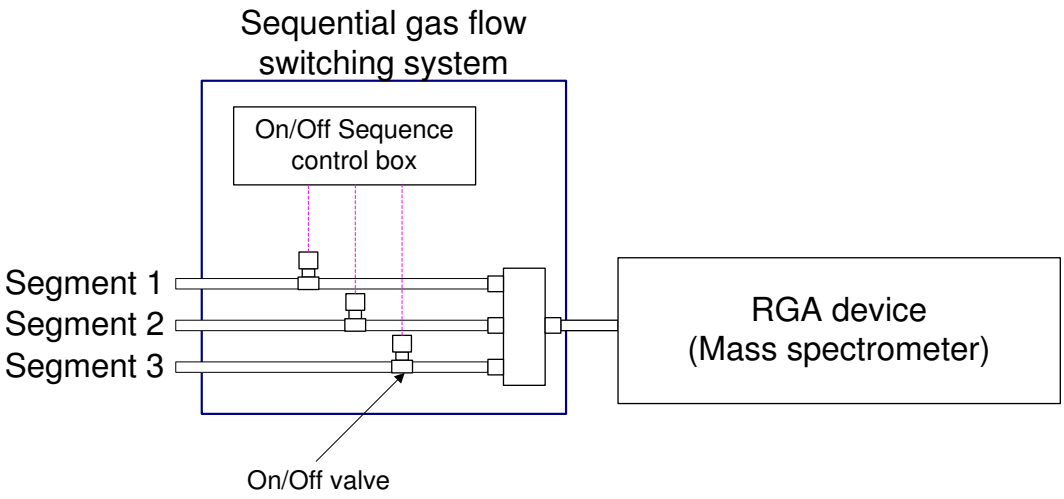

Figure 3.6: Schematic diagram of the time-sharing RGA.

Feed Gas	EXP1			EXP2		
Segment	SEG1	SEG2	SEG3	SEG1	SEG2	SEG3
Ar	30	30	30	60	30	0
H_2	24	24	24	0	24	48
WF_6	6	6	6	0	6	12
total [sccm]	60	60	60	60	60	60

Table 3.2: Experimental feed gas recipes for uniform and non-uniform W deposition.

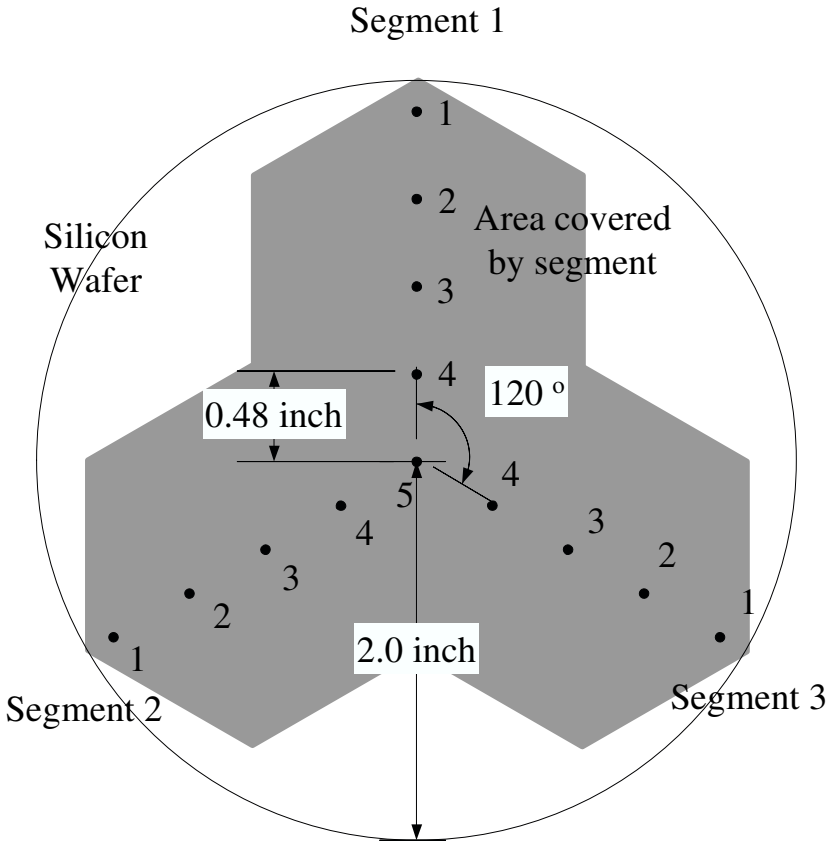

Figure 3.7: The position of thermocouples on the wafer relative to segment/positions.

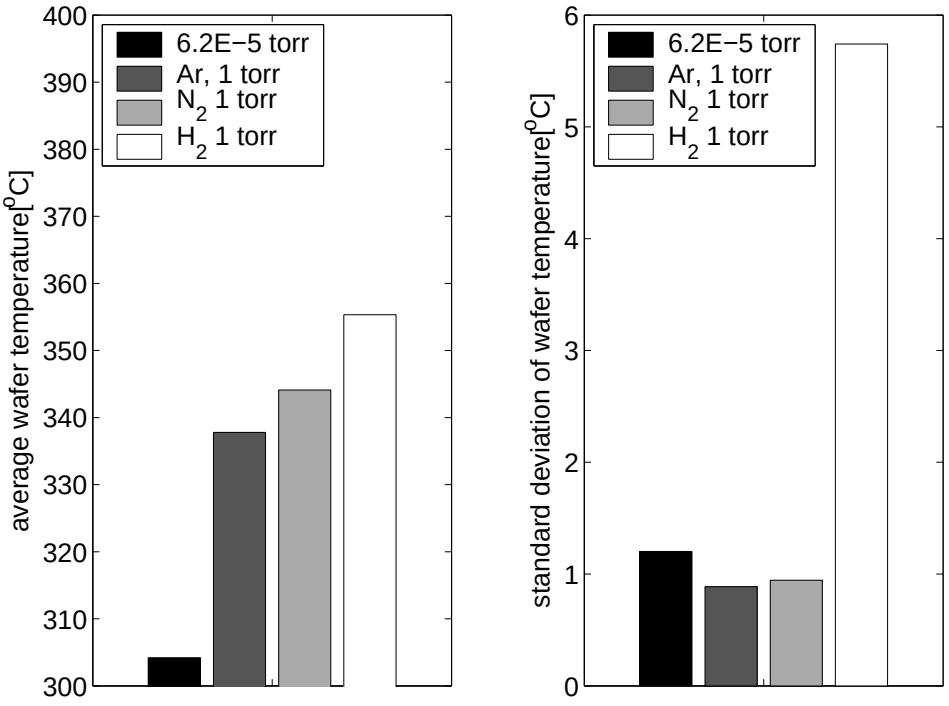

Figure 3.8: Wafer temperature when the reactor is filled with different gases (Ar, N2, H2) at the 400 ^{o}C heater setpoint.

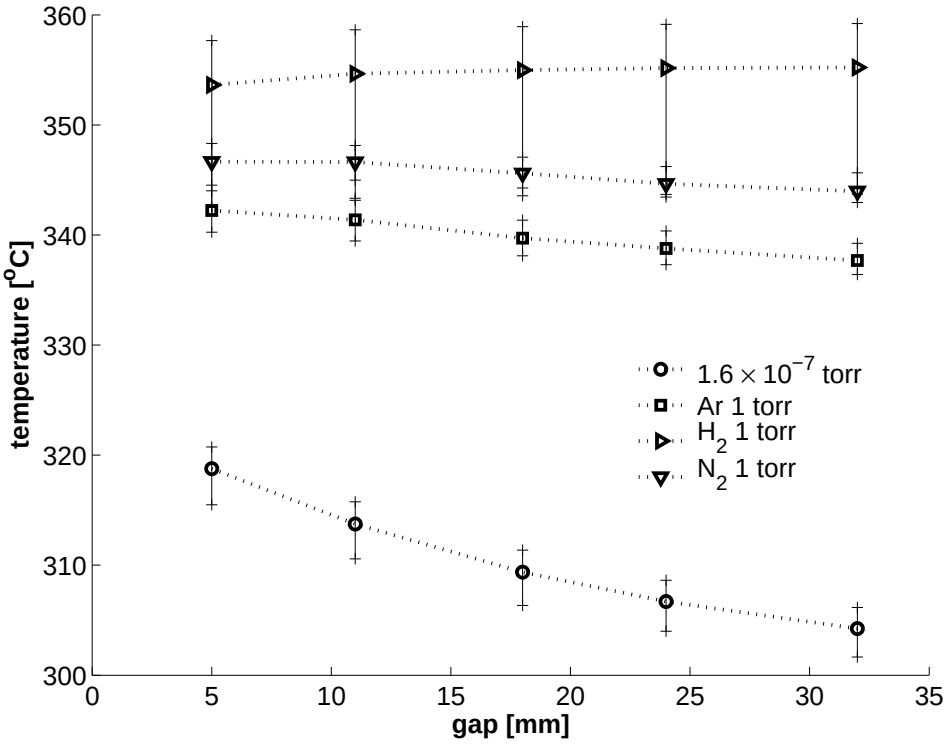

Figure 3.9: Wafer temperature profile with varying wafer/segment gap size, at the 400^{o}C heater setpoint.

The resistance measurements are converted to film thickness based on the assumption that the resistivity of W film is same as bulk W resistivity - it is noted that this assumption is not strictly valid because W films produced by CVD have 1.5 to 2 times higher resistivity than bulk W. However, this measurement is still acceptable for comparing deposition performance of each segment and to evaluate uniform deposition ability because the conditions of each segment are sufficiently similar to produce W films having a similar range of resistivity in this experiment.

The map of thickness measured by the 4 point probe is shown in Figure 3.10. According to the measurements, sharp hexagonal W deposition patterns reflecting the segment locations were observed on the wafer surface, demonstrating clearly the ability of the segments to maintain gas concentrations that differ from that outside the segments.

To assess the uniformity of W film deposited by the prototype P2 reactor, each segment region is measured individually. In Table 3.3 and Figure 3.11, the average thickness and standard deviation of W films based on the 4 point probe measurements are summarized. According to these measurements, the average of W film thickness in each segment is approximately 159 nm. The standard deviation of the overall measurements is approximately 20 nm and this is close to the individual segment's standard deviation of W film thickness. Uniformity of segment-to-segment thickness can be represented by the average and standard deviation of these average thickness values, which are 158.65 nm and 4.06 nm, respectively. Based on this analysis, prototype P2 is able to produce W films which have 2.6 % segment-to-segment and 12.6 % intra-segment uniformity. Segment-to-segment uniformity is an

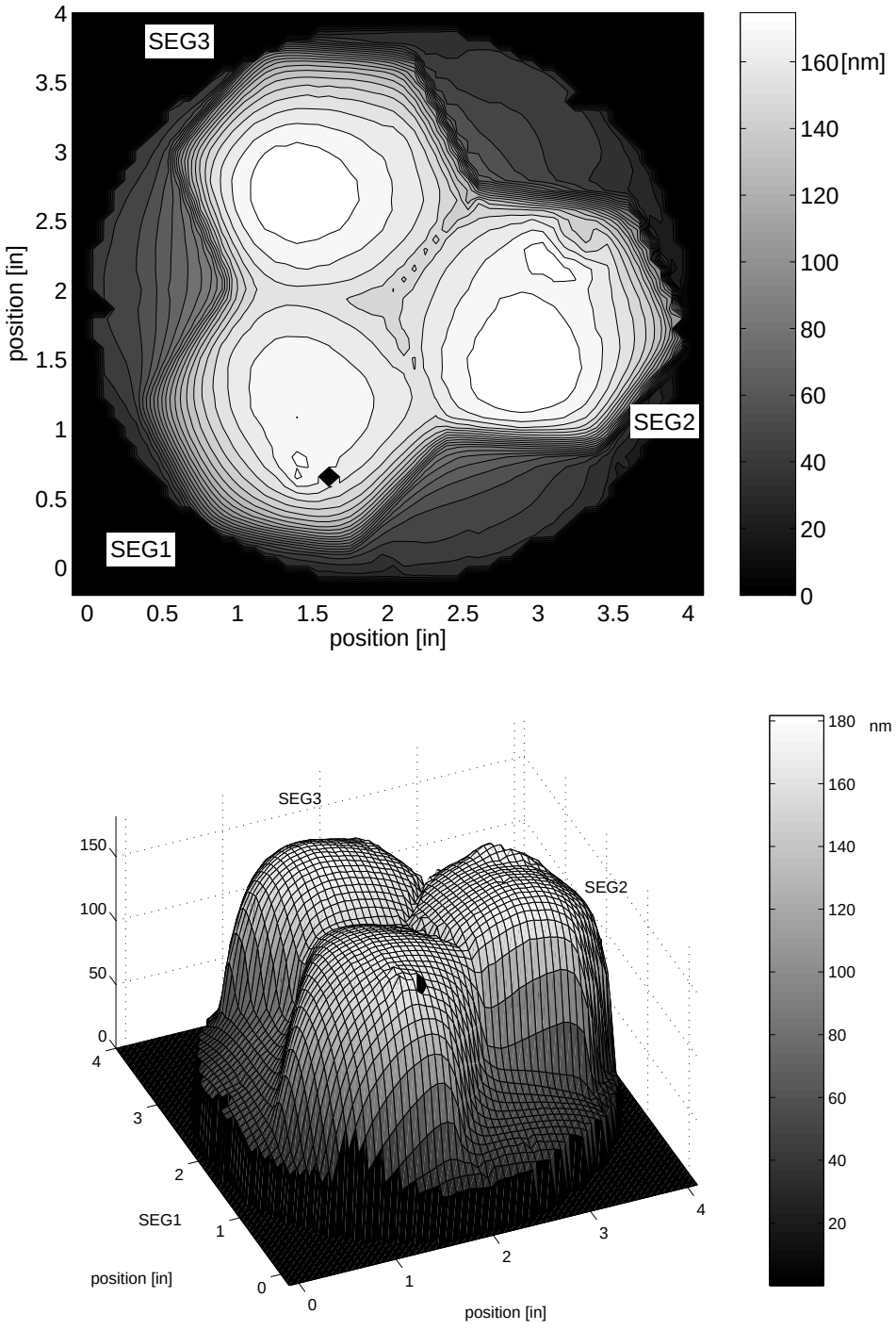

Figure 3.10: Contour map of tungsten film thickness deposited by H_2 reduction (top); 3 dimensional thickness profile of tungsten film (bottom) for EXP1.

index showing performance differences of the segments. Because the performance of each segment is similar, the intra-segment uniformity remains a key index to be improved.

In Figure 3.12, the temperature profile (top) produced using a 5 mm gap and the thickness profile of W films (bottom) are shown. The temperature profiles in Figure 3.12 are measured at the points 1 to 5 in each segment as shown in Figure 3.7. The W film thickness profiles in Figure 3.12 are interpolated values along the line segments intersecting the 5 temperature measurement points in each segment region. The temperature profiles shown in this figure are measured at 1 torr H_2 without gas flowing and a 5 mm wafer/segment gap size and conditions otherwise similar to that of the deposition experiment. Comparing the temperature and thickness profiles, similar patterns were observed. One can immediately infer that intra-segment uniformity depends on the temperature distribution across the wafer as well as the gas composition at the wafer surface. Further experiments are underway, as well as the investigation of design modifications, to improve intra-segment uniformity.

In the comparison of average film thickness of each segment, overall uniformity of W film strongly depends on the intra-segment uniformity. Thus, research focused on improving intra-segment uniformity is necessary to improve overall uniformity of film deposition.

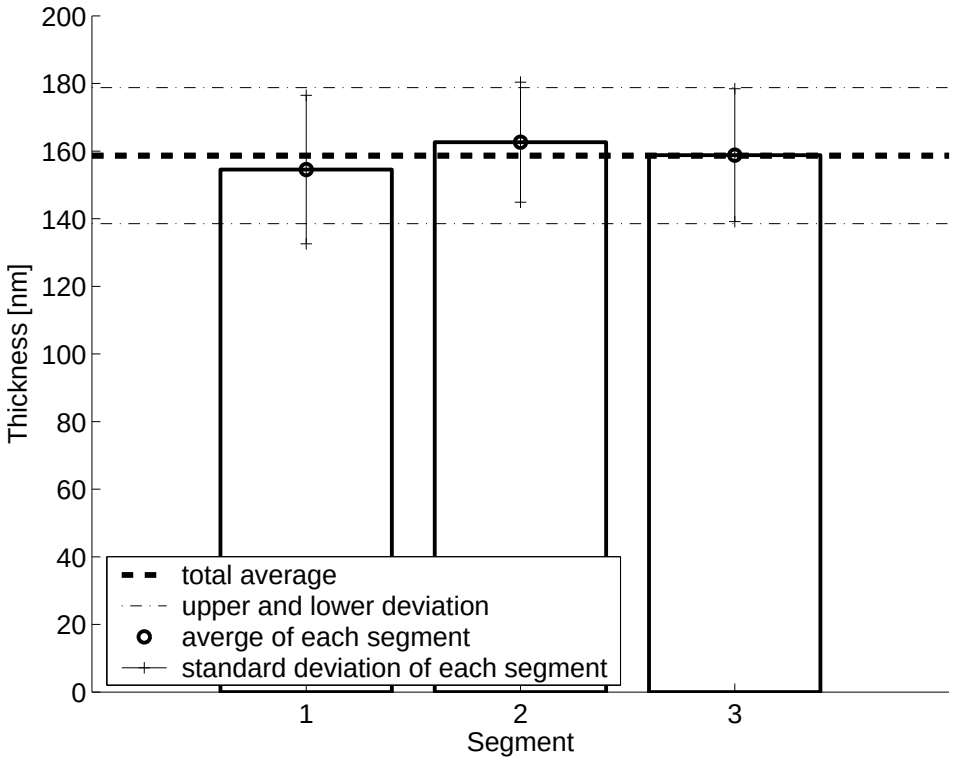

Figure 3.11: Average thickness of W film produced by programmable CVD reactor P2 with recipe EXP1.

	SEG1	SEG2	SEG3	Overall
number of measured points	544	550	550	1644
average thickness [nm]	154.5	162.6	158.8	158.6
standard deviation[nm]	21.97	17.74	19.64	20.12

Table 3.3: Average and standard deviation of W film thickness measurement by 4 point probe resistance measurements.

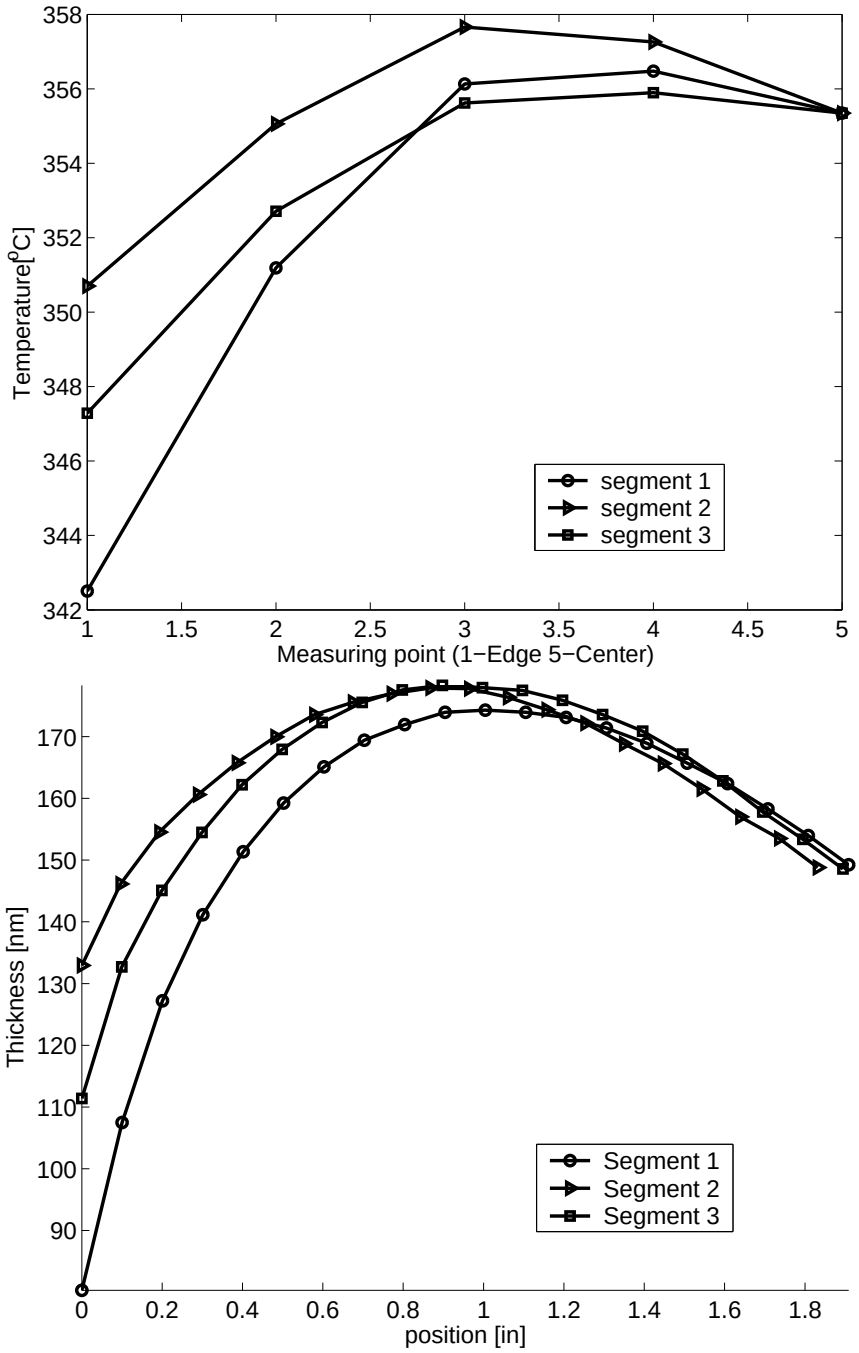

Figure 3.12: Comparison between wafer temperature profile at 5mm gap, 400 ^oC and 1 torr stagnant H_2 (top) and deposition profile (bottom) along the line segments defined by thermocouple positions, for the EXP1 condition.

3.4.3 Non-uniform deposition experiment

To test the concept of programmability of the prototype P2, the intentional non-uniformity producing deposition experiments were performed using the recipe EXP2 in Table 3.2. The experiments results are shown in Figure 3.13. As shown in this figure, the W film grown in segment 1 is thinner than that of the other segment regions but thicker than that found outside of the segment region on the wafer surface. The reactive gases, H_2 and WF_6 are introduced to segment 1 by back by diffusion from the common exhaust volume and diffusion through the wafer/segment gap between segment 2 and 3. The thickness difference between the W film in segment 1 and the outside region can be used as evidence to conclude that the contribution of the precursor gas species by back diffusion from the common exhaust volume is significant.

In the Figure 3.13, it is observed that the gradient (denoted by arrows) of the film thickness in segment 1 is distinctly different from the other segments. This gradient is a partial indicator of the diffusion in which reactant gases diffuse across the wafer surface. From the directions of the gradient, it can be concluded that more reactive gases in segment 1 diffuse from segment 3 than segment 2 because segment 3 has a higher concentration of reactive gases, H_2 and WF_6 compared to segment 2. It is expected that by varying the wafer/segment gap size and concentration of reactive gases in segment 2 and 3, the diffusion pattern, film growth rate, and thickness gradient can be controlled.

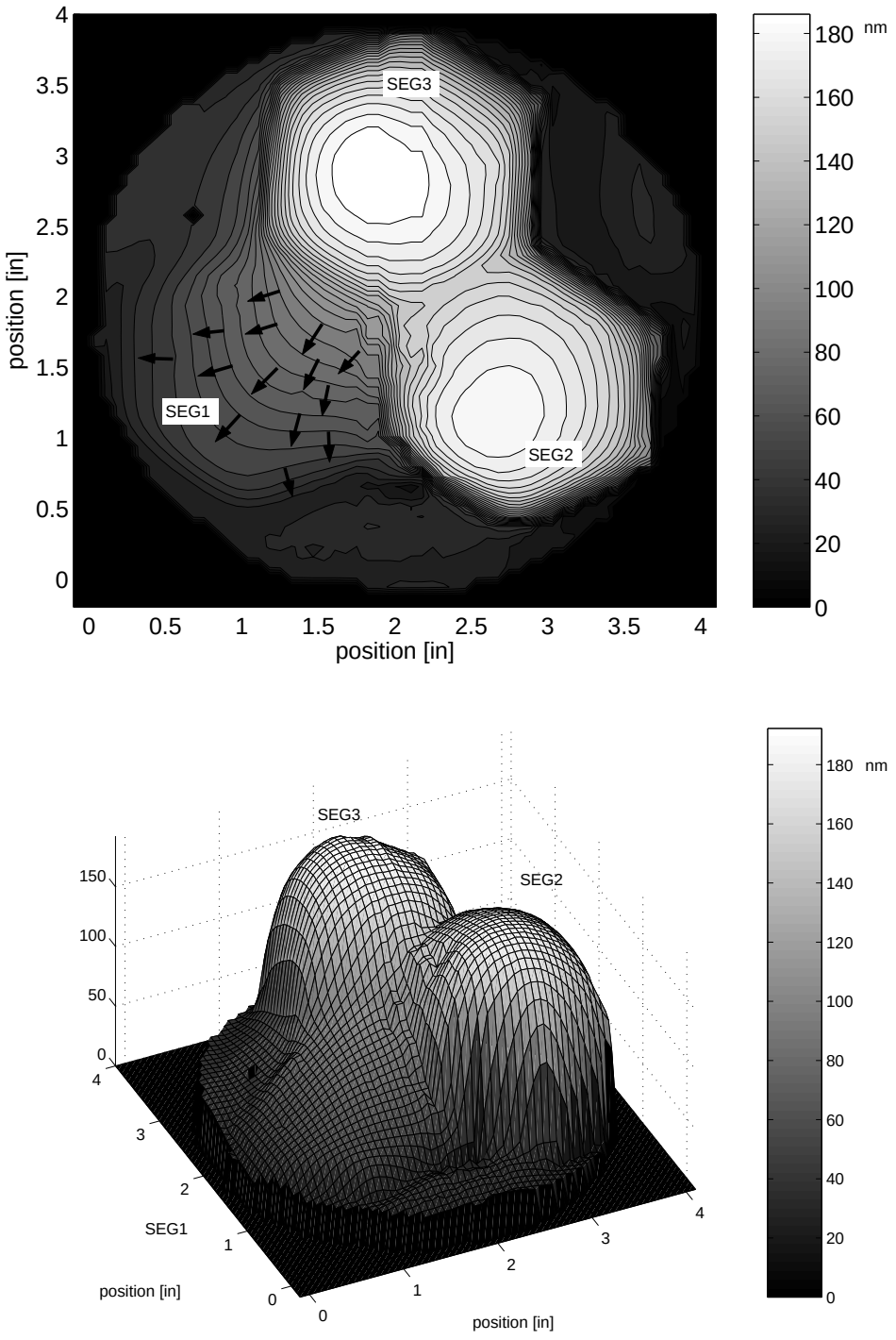

Figure 3.13: Contour map of tungsten film thickness deposited by H_2 reduction (top); 3 dimensional thickness profile of tungsten film (bottom) for EXP2.

3.4.4 W film properties produced by the prototype system P2 using EXP2 recipe

The electrical and physical properties of W film deposited by CVD methods usually depend on the thickness of W film, growth rate, and species of gas used in the process [43] [40]. Particulary, the resistivity of W film deposited by CVD is usually higher than that of bulk W because of impurities (such as the remaining F atoms from precursor gas, WF_6) and small grain size. The faster grown W film has larger grains and fewer F atoms in the films, and thinner W films have smaller grain size. This leads to the general observation that faster grown thick W films have lower resistivity than slow grown W films [42] [40] [43]. In this EXP2 experimental condition, because the W films have significantly different thicknesses, growth rates and processing recipes in each segment, the W film thickness measured by a 4 point probe cannot be used directly to assess segment-to-segment and intra-segment uniformity.

To compare W film thickness measured by the 4 point probe with true thickness measurements, a SEM (scanning electron microscope) is used to take cross sectional pictures of the W film and the Si wafer. SEM allows relatively accurate direct measurement of W film thickness on a Si wafer; however, to take cross sectional pictures, the wafer must be cut into pieces, and so SEM cannot produce a thickness map of W film. However, cross section SEM is still one of the most well known and reliable methods for measuring film thickness. In the discussion to follow, the samples for the SEM are taken from the center of each segment.

The W film thickness measured by SEM and 4 point probe resistance measure-

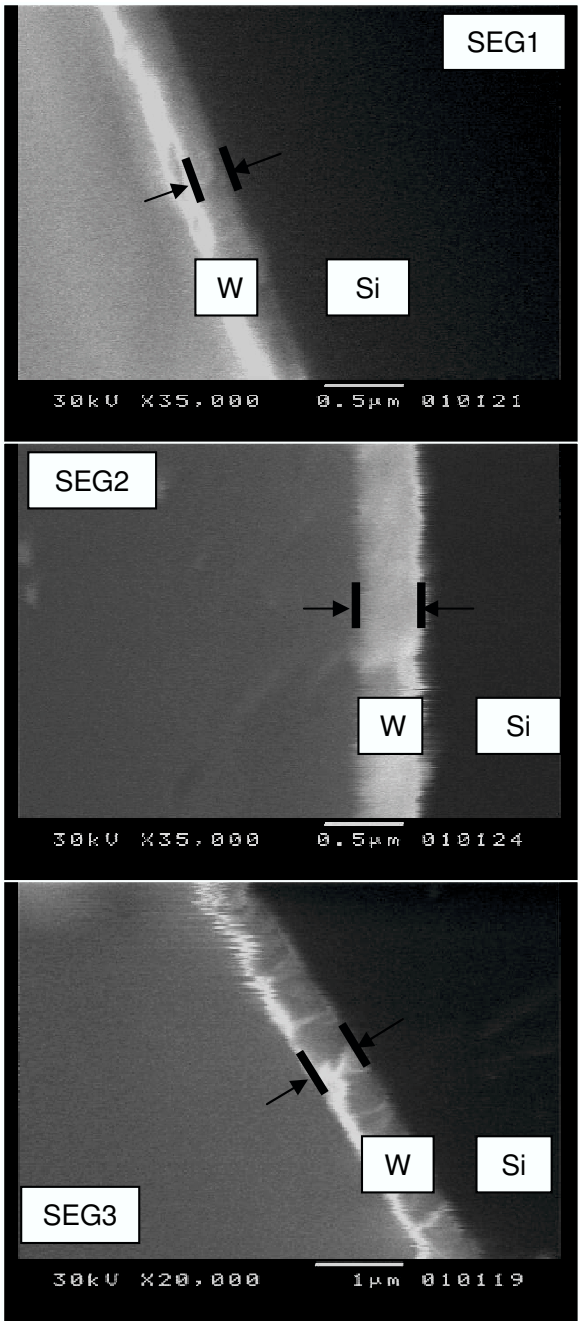

Figure 3.14: Cross section of W films by SEM: Segment1 (top), Segment2 (middle) Segment3 (bottom).

ments are summarized in Table 3.4. The true W film resistivity of each segment is calculated from a comparison of the 4 point probe and SEM measurements and is shown in third column of Table 3.4. According to the calculated results, W films in segment 2 and 3 regions exhibit a lower resistivity relative to that of segment 1. The faster growing W films in segment 2 and 3 have larger grains. As shown in Figure 3.15, grain size of W film in segment 1 is much smaller compared to the two other segments. This is a demonstration that programmable CVD system can produce thin films having different electrical and physical properties in a single batch process.

3.5 **Chapter Summary**

In this chapter, an overview of the design and operation of a highly controllable CVD reactor system was presented. By the control of gas phase composition in a representative deposition process, the potential of this system for performing combinatorial CVD investigations was demonstrated. In particular, an experiment in which inert gas was fed to one of the three showerhead segments resulted in a gradient of film thickness inside this segment region as a result of precursor diffusion from adjacent segments. While this gradient was limited to the one segment region in this experiment because of the small gap size used, future experiments will be performed where larger gap sizes will be used to diffuse this gradient across multiple segment regions. It is from combinatorial experiments such as these that a desirable film quantity will be identified; the process conditions at this spatial point on the wafer will be determined from the reactor simulator and the reactor system then

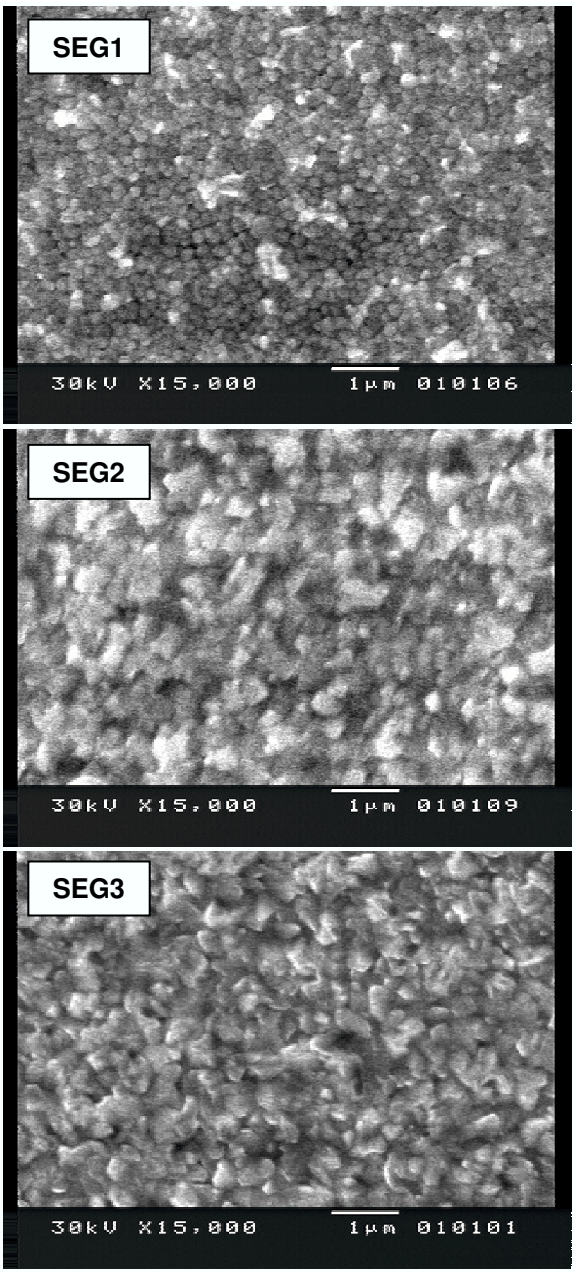

Figure 3.15: Surface of W films by SEM: Segment1 (top), Segment2 (middle) Segment3 (bottom).

will be reprogrammed to deposit this desired film uniformly over the wafer surface.

In the uniform and non-uniform thin W film deposition experiments with this new P2 system, the spatial controllability of this reactor system was demonstrated with segment-to-segment and intra-segment uniformity assessment. However, accurate thickness measurements and further investigation of W film properties are necessary to ultimately enhance the programmable capabilities of this new CVD reactor system.

The new prototype P2 system has the capability to deposit W films using spatially nonuniform recipes such as EXP2 in Table 3.2. With this intentional non-uniform deposition capability, programmable CVD system can be a candidate tool for combinatorial material discovery research tool.

Segment	4 Point Probe [nm]	SEM [nm]	Resistivity [$\mu\Omega$ cm]
SEG1	56.2	270	26.88
SEG2	146.1	420	16.10
SEG3	180.7	580	17.97
Bulk W	-	-	5.6

Table 3.4: Thickness and resistivity measured by 4 point probe resistance measurement and scanning electron microscopy.

Chapter 4

Conclusions

In chapter 1, the limitations of conventional CVD reactors due to inflexible designs and lack of control actuators were discussed, and new reactor system concepts endowing spatial controllability as a means of overcoming these limitations were introduced. The feasibility of these design concepts were tested with simulation, and the key design factors and operation parameter values were identified, such as the wafer/segment gap, feed tube position, and total feed rate.

In chapter 2, the first prototype reactor was designed based on the simulation results discussed in chapter 1, and was constructed for performing preliminary deposition experiments. In chapter 2, the results of preliminary deposition experiments demonstrated that spatially patterned wafers can be produced by the Programmable CVD reactor. These experimental results were compared to the simulation results of a rigorous model. By this comparison, the contribution of back diffusion and inter-segment diffusion through wafer/segment gap was estimated. By these preliminary experimental and simulation study, it is revealed that back diffusion can contribute more to interaction between segments than inter-segment diffusion especially when segment is at low position.

For the modeling and simulation, Maxwell-Stefan equation was used to describe behaviors of feed gas mixture. The inter-segment flux equations (three equation for each segment) are solved simultaneously with the same number of collocation-discretized Maxwell-Stefan equation subjected on to the boundary conditions by using a Newton-Raphson method. In this model, thermal diffusion ex-

pression is also included as well as ordinary diffusion equation. This Maxwell-Stefan equation is considered very rigorous and accurate method to model complex gas mixture. But this Maxwell-Stefan equation is not often used in commercial simulation package because this Maxwell-Stefan equation is often solve after significant number of iteration. To avoid significant number of iteration calculation without losing its rigorousness and accuracy, the 1-dimensional model for the programmable reactor segment used for the simulation is suitably simplified.

To set up the simulator, object oriented approach was taken. This object oriented approach was efficient for the simulation because the modeling equations for each segment are identical in structure. Also the simulator set up by this object oriented approach is extensible to reactor model with many more segments as mentioned in chapter 2. The successful simulation results of this work showed that this object oriented approach is efficient and applicable for the systems having repeated elements in structure.

In chapter 3, a second prototype reactor system design described that included a gas delivery system allowing the programmability of gas composition control, a UHV grade chamber and pump system minimizing contamination, and a gas sampling system allowing multiple 2-dimensional sensing across the wafer. Uniform and intentionally non-uniform W films deposition by H_2 reduction were performed to demonstrate true 2-dimensional controllability. The programmability introduced and demonstrated in this chapter is the necessary capability to find efficiently the proper material and the process conditions corresponding with the properties of that material. Also this programmability allow quick reprogramming to achieve uniform

film deposition of that material only with parameters changing.

This research work motivated for lessening the cost to improve thin film deposition uniformity was successfully accomplished by suggesting new control actuator concept which can directly control uniformity of thin film. To maximize the benefit to use these new actuator concepts, the programmability was devised and demonstrated in chapter 3. This programmable CVD reactor system concept is unique and successful in terms of its direct spatial controllability, and has potential to be applied for any system controlling the gas delivery on solid or liquid surface.

Chapter 5

Future work

In this chapter, future work for achieving the ultimate goal of this research is discussed. First, necessary tests and experiments for improving intra-segment film deposition uniformity will be discussed. Second, a control strategy maximizing utilization of programmability will be presented.

5.1 Improving Intra-segment Uniformity

In the programmable CVD reactor, overall film uniformity reflects segment-to-segment uniformity and intra-segment uniformity. As shown in chapter 3, intra-segment uniformity appears more strongly related to the overall uniformity of W film thickness across the wafer rather than segment-to-segment uniformity in second prototype programmable CVD reactor, P2. In Figure 5.1, two cases demonstrating improved intra-segment uniformity and segment-to-segment uniformity are shown. Also, it is shown that the overall uniformity improvement can be achieved by improving both intra-segment and segment-to-segment uniformity.

Temperature distribution and gas concentration across the wafer inside a segment region directly relate to intra-segment film uniformity. Thus, the parameters affecting these two factors should be tested in various ranges of experimental conditions as a first step towards improving intra-segment uniformity.

Because the wafer/segment gap size is an important factor affecting gas composition in the segment-to-segment boundary area [35] as well as temperature distribution, deposition experiments with varying gap size must be investigated for

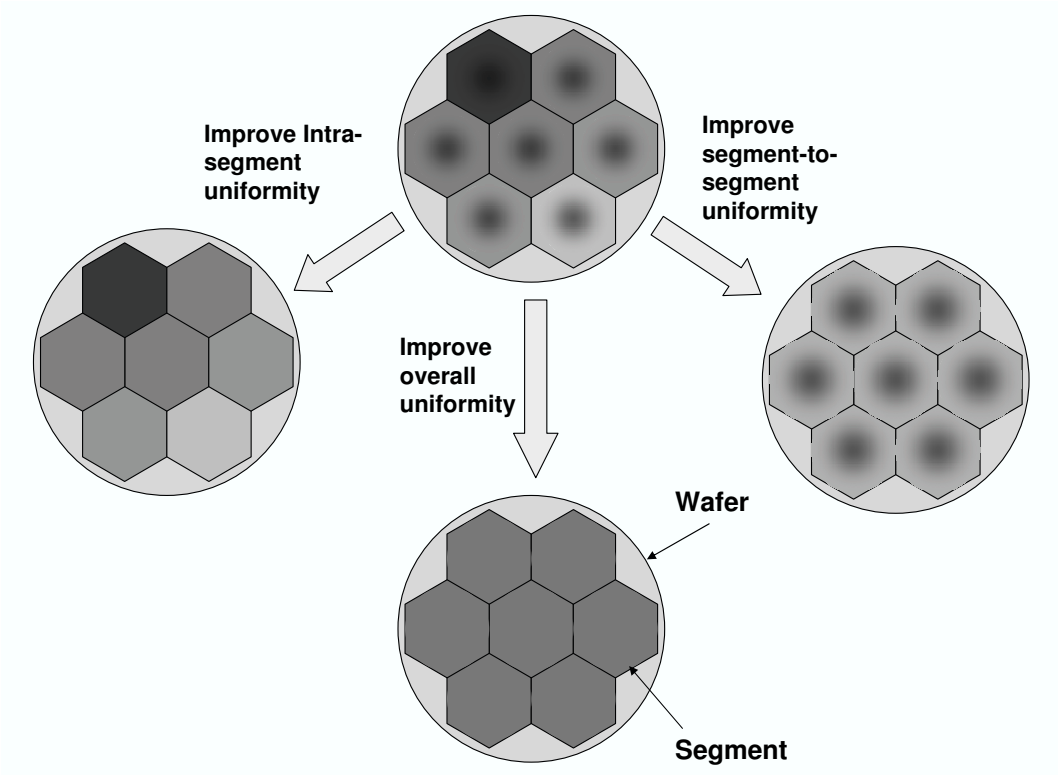

Figure 5.1: Factors leading to overall uniformity improvement

improving intra-segment uniformity. With the larger gap size, a more uniform W film can be produced (note Figure 1.4).

Because the simulator described in chapter 2 was based on the 1-dimensional model, it is limited in accuracy to compare the thickness of W film predicted by this simulation with average W film thickness of experiments in each segment. To properly use this model and simulation for improving intra-segment film uniformity, 2 or 3-dimensional model is necessary. To develop a 2 or 3-dimensional model and simulation, validating the model and its parameters for describing W film growth rate, diffusion, and convection transport should be performed. Once the model's parameters are decided, then a simulator capable of predicting 2 or 3-dimensional gas composition distribution across the wafer surface can be available. Also this new simulator based on 2 or 3-dimensional model can be used to reveal the relationship between film composition and gas composition on wafer surface for combinatorial CVD research.

5.2 Control Strategy for the Programmable CVD System

As discussed in chapter 1, in a conventional CVD reactor, the uniform film deposition across larger wafers is more difficult because of non-flexible designs that lack spatial controllability. With the programmable CVD reactor, the effect of wafer size on across wafer uniformity can be minimized, because the programmable reactor divides the wafer surface area into smaller areas in which film deposition can be controlled individually, minimizing the interaction with other areas. Thus, in the Programmable reactor concept, more segments are needed to achieve uniform

deposition across larger wafers.

The multiple sensing capability of the programmable CVD reactor allows direct uniformity monitoring with mass-spectrometer RGA which is impossible in a conventional CVD reactor system. As a result, two different control strategies can be applied to decouple deposition uniformity with wafer size to improve uniformity from the control of other material characteristics. This control concept is discussed next.

5.2.1 Measurement based optimal control

In the programmable reactor, performance of a segment is related to that of other segments surrounding the segment. Also, the important indices representing film qualities, such as uniformity and the physical properties of the film, are related and conflict with each other. Finding a operating condition satisfying all desirable index values often is not achieved. Thus, an optimal control approach, in which finding a condition minimizing the deviations from a target value, is necessary. For example, in W film deposition, uniformity and resistivity are two indexes of film quality. The objective function to be minimized is represented by following equation:

$$O(\mathbf{C}) = W_u(U_t - U_f(\mathbf{C}))^2 + W_R(R_t - R_f(\mathbf{C}))^2 \tag{5.1}$$

where W_u and W_R are weights, U_t and R_t are target values of uniformity and resistivity, respectively, and U_f and R_f are measured film values of uniformity and resistivity, respectively. $\mathbf{C}$ is the vector of manipulated variables (control inputs). Thus, the goal of the control is to minimize the objective function

$$\min\{O(\mathbf{C})\} = \min\{W_u(U_t - U_f(\mathbf{C}))^2 + W_R(R_t - R_f(\mathbf{C}))^2\} \tag{5.2}$$

Because the indexes representing film quality relate to each other in complicated and often nonlinear relationships of the operation parameters, developing a proper mathematical model is very challenging. Also, uncertainties such as wafer surface condition, unmeasurable wafer temperature distributions, and gas feed rate variations can cause model mismatch in model-based optimal control. Thus, instead of developing a physical model for model-based optimal control, a measurement-based optimal control approach may be more effective.

5.2.2 Multiple endpoint detection

Endpoint detection is one of the rising methods in advanced process control of semiconductor manufacturing and is used for deciding the termination point of etch and deposition processes. Research on endpoint detection applied to W CVD is reported in [25] [37] [38] [44]. In endpoint detection, the status of the film thickness and film growth rate is detected using the integrated RGA signal sampled from the process chamber or gas exhaust line. Stoichiometric and statistical analysis tools convert the integrated signal of reaction byproduct gases into film thickness. Thus, when this integrated signal reaches the desire thickness level, the process is terminated.

RGA sampling tubes installed in each segment of the programmable CVD reactor and timesharing manifold allow the multiple sampling. From the integrated RGA signal of each segment, multiple endpoint detection allows monitoring of growth rate

and average W film thickness deposited in each segment region. Based on endpoint detection in each segment, termination of recipe gas feed for each segment is decided instead of termination of the entire process. If a recipe gas feed is terminated, the same amount of inert gas is fed to minimize convective interaction caused by flow rate differences between segments. The conceptional diagram of multiple end-point control is shown in Figure 5.2.

5.2.3 Combined measurement based optimal control and multiple endpoint detection

The two different control strategies described previous sections can be combined to decouple the film property control and uniformity control. Usually, the control parameters for film quality, such as feed gas recipe, wafer temperature and reactor pressure also affect uniformity. Because of this complicated interaction, it is hard to decouple film quality control and uniformity control. However, in the programmable CVD reactor, uniformity can be controlled without affecting film property using multiple endpoint detection. Similarly, film property also can be controlled by measurement based optimal control without affecting uniformity. The schematic diagram of combined control strategy is shown in Figure 5.3.

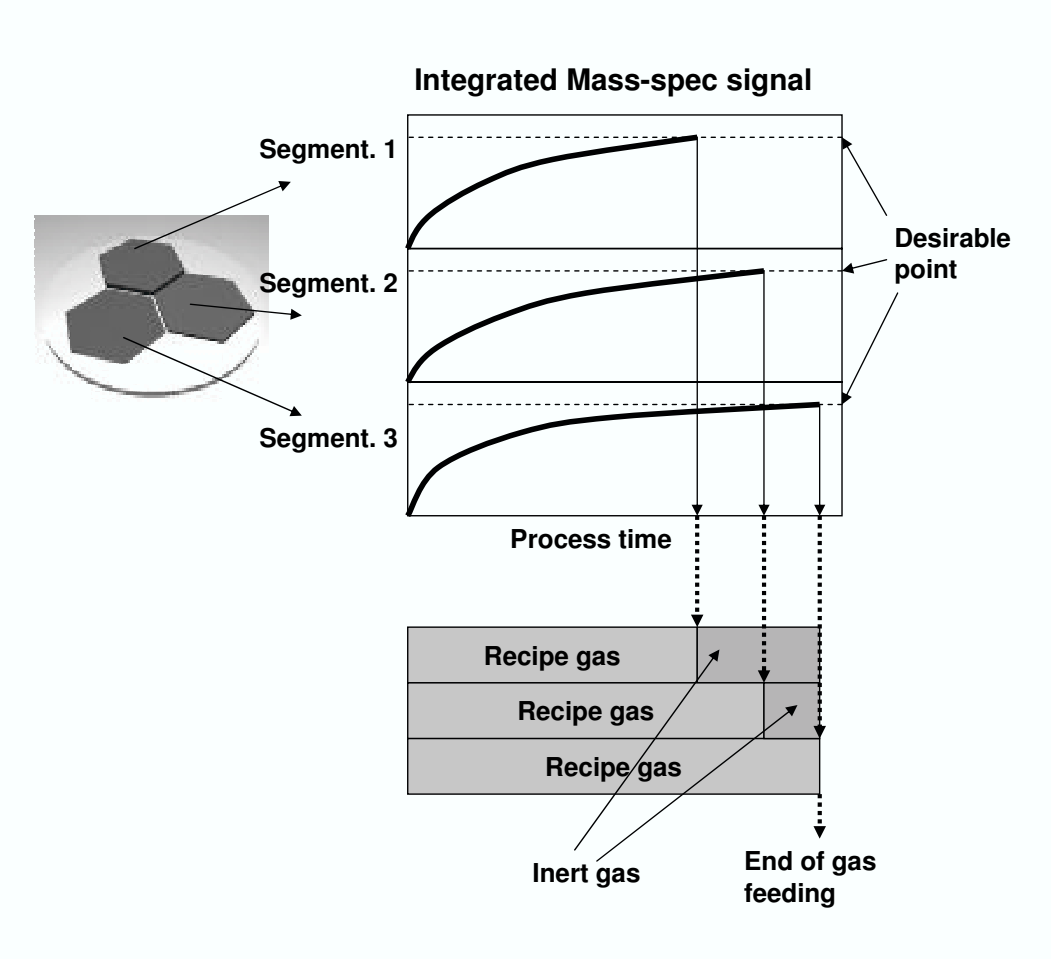

Figure 5.2: Scheme for the multiple endpoint detection for the programmable CVD system.

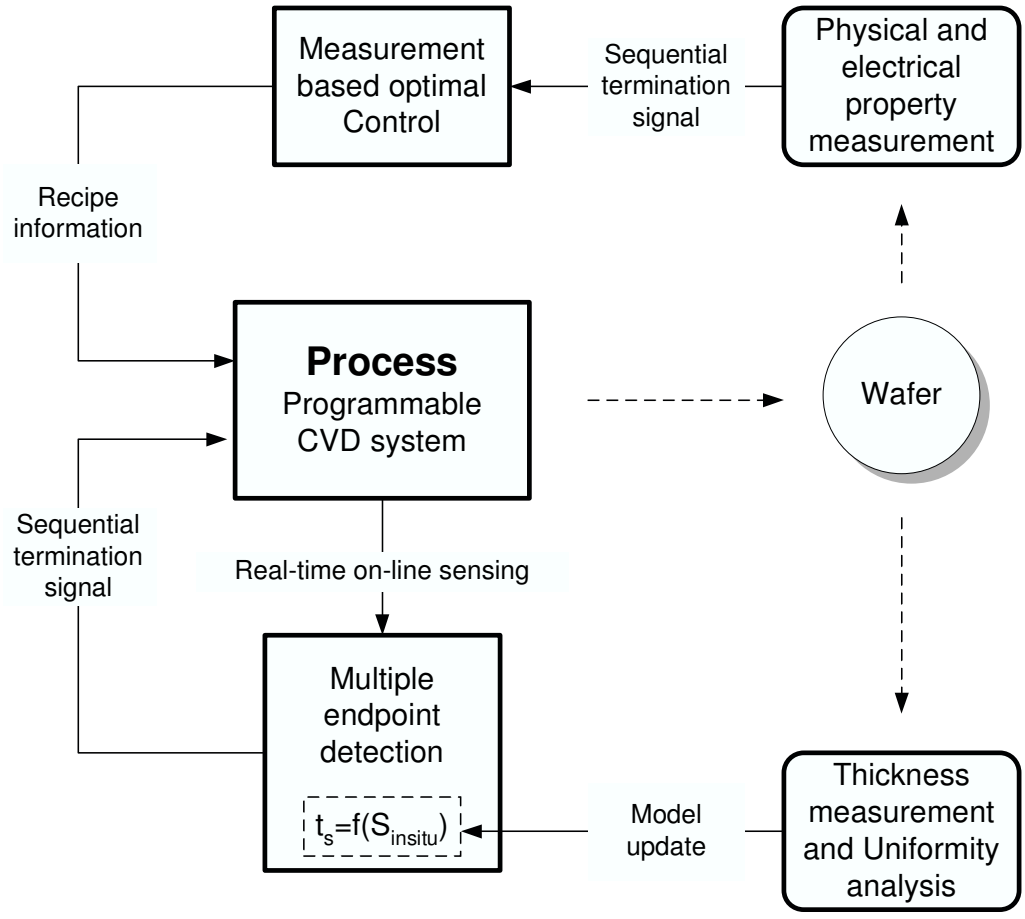

Figure 5.3: Combined control scheme for the programmable CVD system.

Appendix A

W Chemical Vapor Deposition

Tungsten is widely used for interconnects in the semiconductor device fabrication because of its high melting point, low electrical resistivity, and a thermal expansion factor that is close to that of Si. W is mainly deposited as a contact plug and first-level metal by chemical vapor deposition because W films deposited by CVD have very good step coverage [41].

A.1 W CVD chemistry

W CVD is the most successfully established metal CVD process in semiconductor fabrication because the WF_6 precursor is relatively stable and easily reacts with various gas and solid species such as Si, SiH_4, H_2, Al, and Ti, etc. Among these chemical species, SiH_4 and H_2 are commercially important reducing agents as well as solid Si. The chemistry of WF_6 with these species are listed below [42]:

$$WF_6(g) + SiH_4(s) \longrightarrow W(s) + SiF_4(g) + 2HF(g) + H2(g)$$

$$2WF_6(g) + 3SiH_4(s) \longrightarrow 2W(s) + 3SiF_4(g) + 6H2(g)$$

$$WF_6(g) + 3H_2(s) \longrightarrow W(s) + 6HF(g)$$

$$2\ WF_6(g) + 3Si(s) \longrightarrow 2W(s) + 3SiF_4(g)$$

The reactivity of WF_6 with a reducing agent is determined by the Gibbs free energy changes in the reaction. The free energy changes of these reactions are shown in Table A.1 [42]. The most preferred chemical reaction of WF_6 is with SiH_4. Thus the reaction rate with SiH_4 is faster than the other reactions listed.

By SiH_4 reduction, thin films of W can be deposited on Si, SiO_2, and metal

surfaces. Also, W film growth rates are greater for SiH_4 reduction compared to other reduction mechanism. The W film produced by SiH_4 reduction is usually less conformal than W film by H_2 reduction, has higher resistivity, and tends to delaminate spontaneously from the Si surface. Usually resistivity of W film deposited by SiH_4 reduction is more than 3 times higher than that of bulk W [40]. Because of this drawback, SiH_4 reduction is mostly used only for W seed layer deposition on an adhesion layer such as Ti/TiN films. H_2 is used as the primary filling process for narrow features such as trenches and vias.

The higher resistivity of W films deposited by CVD is due to the existence of impurity fluorine and the small grain size of W poly-crystal. Bulk W does not have distinguishable grain structure, but CVD W usually exhibits α and β phases of grain structure. Usually, faster reaction processes produce β structure W films which have lower resistivity.

Thus, W plug or via filling normally has several steps in sequence: 1) Hole patterning, 2) Glue(adhesion)/barrier layer deposition, 3) Seed layer deposition, 4) Blanket W deposition, 5) W etchback. The typical W plugging diagram is shown in Figure A.1. As shown in diagram, small sub-micron features, such as a W plug, are mainly filled by blanket W deposition by H_2 reduction. If growth rates of W film in small features across the wafer are significantly different, in faster growing areas, the plugs will be filled inside of feature before others are filled. Often, this feature captures voids which can cause serious damage to the device performance. Thus, uniform film deposition is critical in H_2 reduction W deposition for improving yield of production of micro-electric devices, shown in Figure A.2.

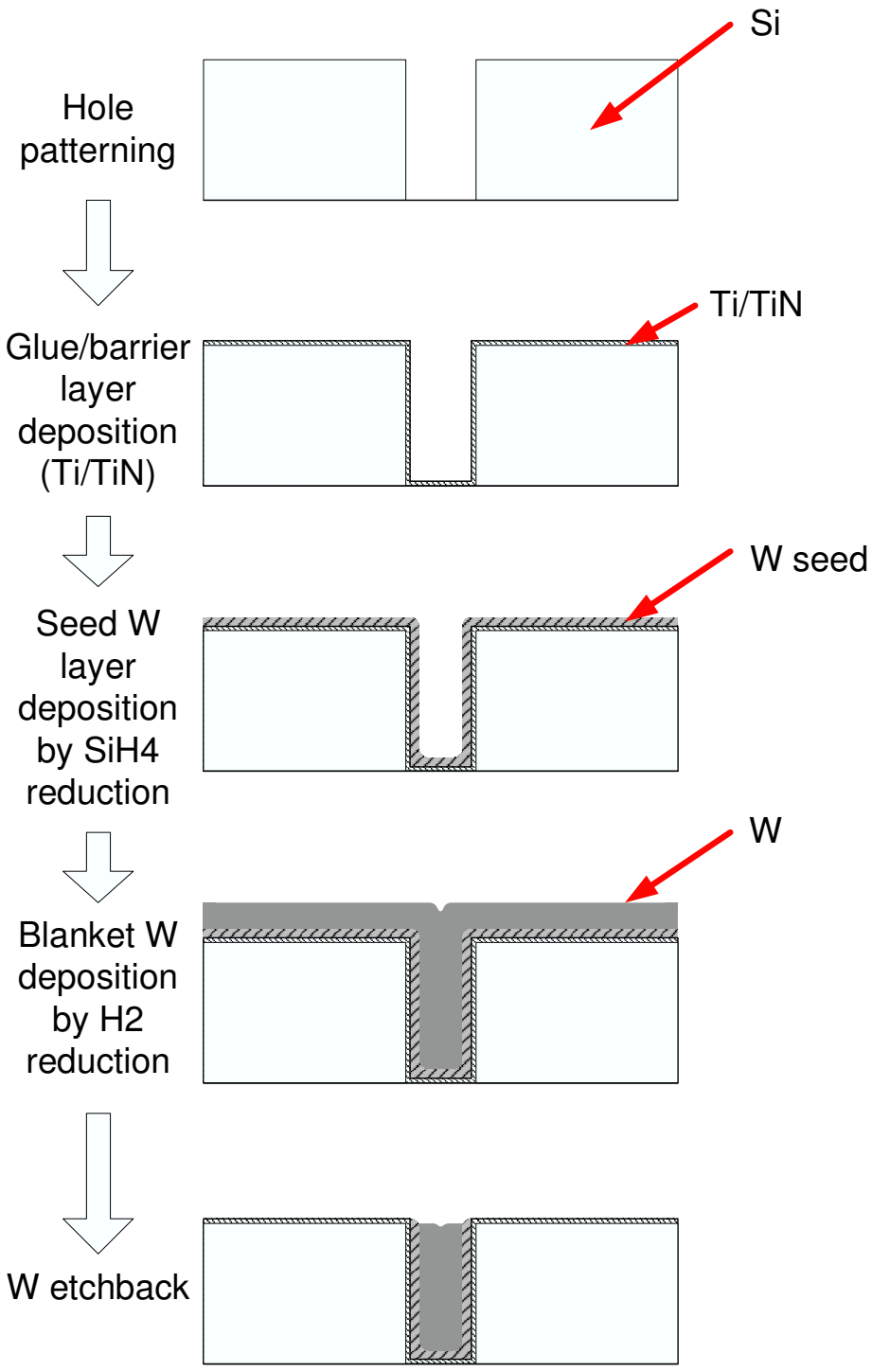

Figure A.1: Typical 5 steps of W filling into narrow features in micro-electrical device fabrication.

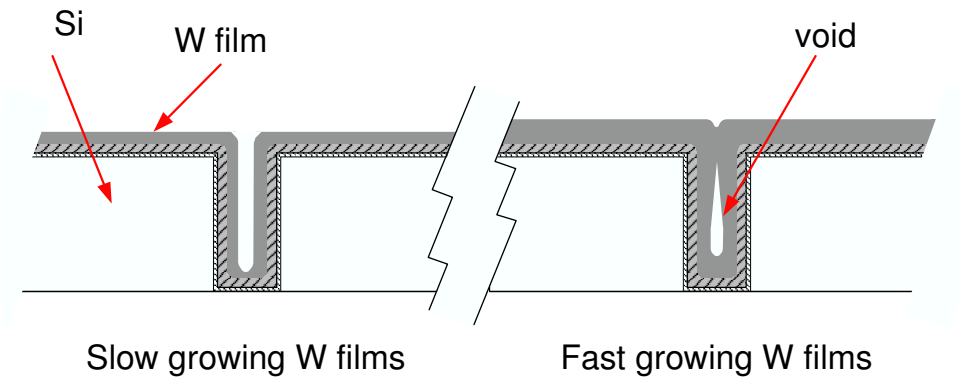

Figure A.2: The void formation in the small feature such as W plug by difference of W film growth rate across wafer.

Reaction	ΔG at 500^oK (KJ/g-atom W)
$WF_6 + 3H_2 \longrightarrow W + 6HF$	-113
$WF_6 + 1.5Si \longrightarrow W + 1.5SiF_4$	-478
$WF_6 + 1.5SiH_4 \longrightarrow W + 1.5SiF_4 + 3H2$	-870

Table A.1: Free energy changes for CVD W deposition.

A.2 Overall growth rate expressions for H_2 reduced W on a wafer surface

Under low pressure and low gas phase temperature conditions, the gas phase reactions between WF_6 and H_2 are negligible [23] [45]. The W growth mechanisms by surface reaction of WF_6 and H_6 consists of five steps. First, reactive gas species diffuse onto the Si surface through the gas phase. Second, these gas molecules are absorbed on the surface and become active. Third, these active WF_x and H_2 react with each other and produce byproduct HF. Fourth, byproduct gas HF, and non-absorbed WF_6 and H_2 desorb from surface. Finally, these residual gases, HF, WF_6 and H_2 are released to gas phase by diffusion. In these five steps, many complex intermediate states exist, however, analyzing all intermediate states can consume significant amounts of research effort. Instead of this models, overall growth model with empirically determined parameters are often more useful for predicting process performance. The most widely used reaction model for W growth by H_2 reduction is based on the following model [46] [47]:

$$R_s = \frac{c_1[H_2]^{1/2}[WF_6]^{1/6}}{1 + c_2[WF_6]^{1/6}} \tag{A.1}$$

If sufficient amounts of WF_6 are supplied to the wafer surface ($1 \ll c_2[WF_6]^{1/6}$), W film growth rate can be expressed by following equation:

$$R_s = (c_1/c_2)[H_2]^{1/2} \tag{A.2}$$

where $(c_1/c_2) = k_a e^{\left(\frac{-E_a}{RT}\right)}$.

If WF_6 supply is not sufficient($1 \gg c_2[WF_6]^{1/6}$), W film growth rate can be

Equation	Symbols	Values	Unit	Reference
A.2	R_s	·	$mol \cdot m^{-2} \cdot s^{-1}$	[23]
	k_a	1.7	$mol \cdot Pa^{-1/2} \cdot m^{-2} \cdot s^{-1}$	
	E_a	69	$kJ \cdot mol^{-1} \cdot K^{-1}$	
A.3	R_s	·	$nm \cdot s^{-1}$	[48]
	k_b	3500 ± 400	$nm \cdot s^{-1} \cdot Pa^{-2/3}$	
	E_b	64	$kJ \cdot mol^{-1} \cdot K^{-1}$	

Table A.2: Parameters and values for the WF_6 growth rate expression of H_2 reduction.

expressed by following equation:

$$R_s = c_1[H_2]^{1/2}[WF_6]^{1/6} \tag{A.3}$$

where $c_1 = k_b e^{\left(\frac{-E_b}{RT}\right)}$.

In the case of very low feed rate of WF_6 or local depletion of WF_6, the second equation is more valid to describe the surface WF_6 and H_2 reaction. But most other case, the first simplified equation is used. Parameters and values for the equations are shown in table A.2.

Appendix B

Thickness measurement of W films using a 4 point probe

The 4 point probe is a device for measuring the resistance of materials using a 4 contact probe built into a sensor head in which the 2 outer probes apply current and 2 inner probes measure voltage. The schematic diagram of probe head is shown in Figure B.1. This 4 point probe is usually used for measuring resistivity of thin films for determining the film thickness. If the film resistivity is already known, resistance measured by 4 point probe can be converted into the thickness of film. The relationship between the thickness, resistivity and sheet resistance of thin films is expressed in following equation when film thickness is sufficiently thinner than the distance between probes ($t_s \ll S$).

$$t_s = \rho \left(\frac{ln2}{\pi} \right) \left(\frac{I}{V} \right) \tag{B.1}$$

4 point probe measurements are relatively simple in terms of sample preparation, operation and converting the measurements to the thickness or resistivity. Also, because 4-point probe's very short measuring time and relatively small size and light weight sensor head, it is easily automated so as to be able to scan an entire wafer surface. Thus, if it is acceptable that W thin film resistivity is considered the same as bulk W resistivity, 4 point probes are very useful devices to map W film thickness in a university lab. The automatic high resolution 4 point probe developed by Rubloff's group in University of Maryland is used for measuring W film thickness in this research and a photograph of it is shown in Figure B.2.

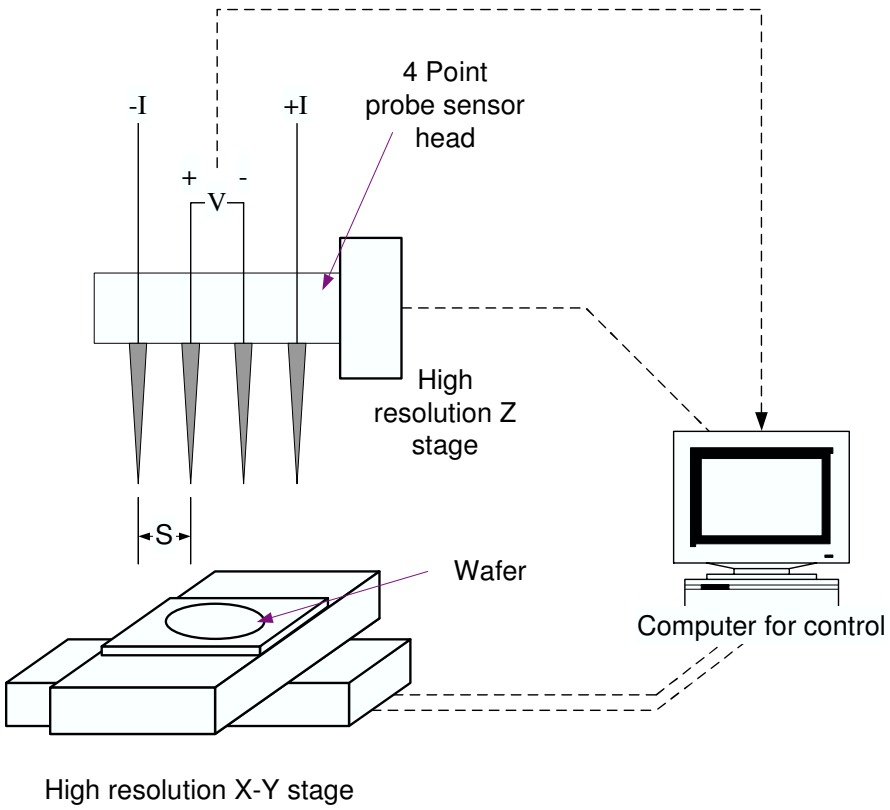

Figure B.1: Schematic diagram of an automatic high resolution 4 point probe station developed at the University of Maryland

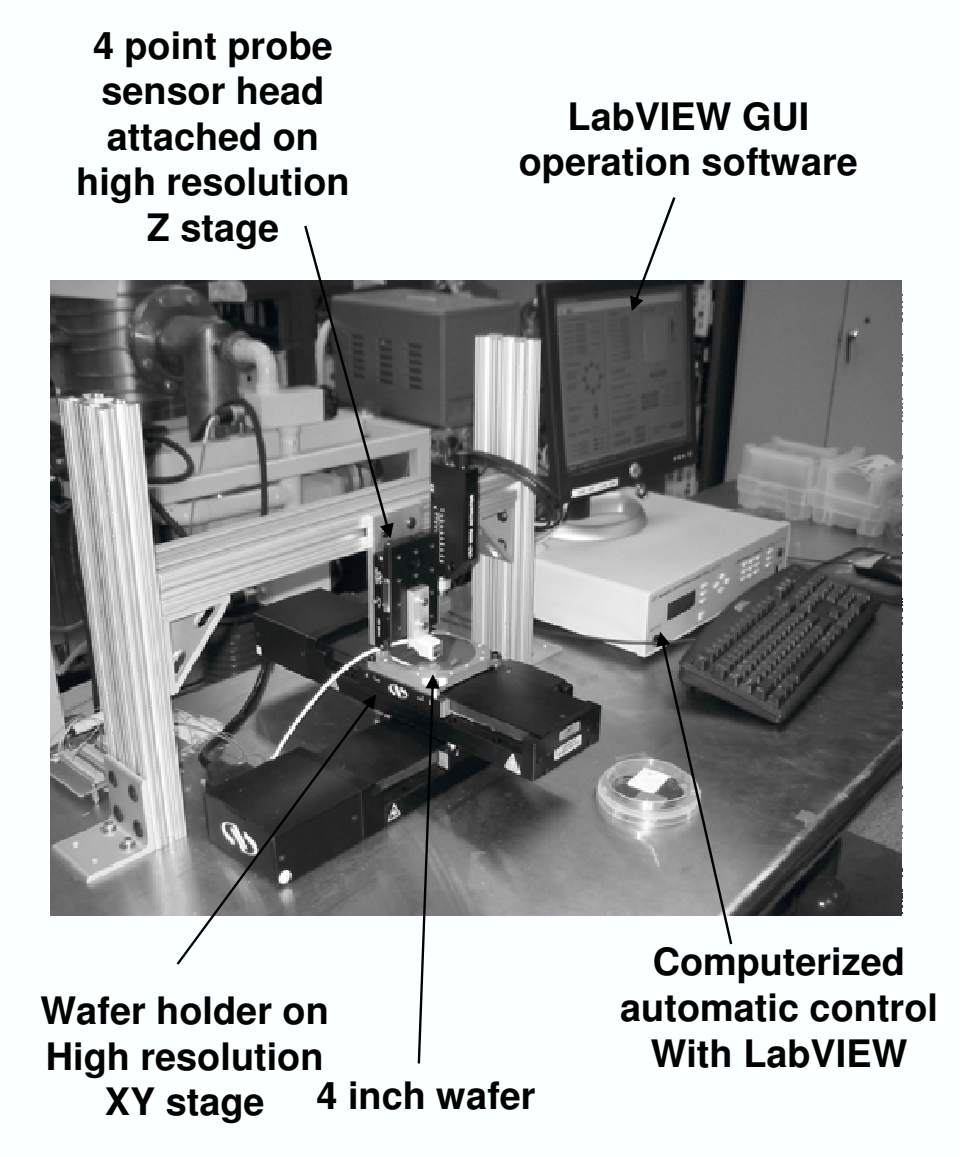

Figure B.2: Photograph of an automatic high resolution 4 point probe developed by Rubloff's group at the University of Maryland

Appendix C

Parameters used for modeling and simulation

Symbol	*Units (and Value)*	*Description*
A_f	$9.5 \times 10^{-5}\ m^2$	feed + sample tube cross section area
A_s	$0.0016\ m^2$	segment cross section area
C	mol/m^3	total concentration
D	m^2/s	diffusivity of Si in W
D_{ij}	m^2/s	gas phase binary diffusion coefficient
D_i^T	$kg/(ms)$	gas phase thermal diffusion coefficient
E_a,E_b		activation energy
f_d		inter-segment transport correction factor
h	m	wafer/segment-bottom gap size
k_a,k_b		collision factor
K^k	nm/min	W deposition rate coefficient
L	$0.144\ m$	segment length
M_i	kg/mol	species i molecular weight
N_i^k	$mol/(m^2s)$	species i segment k total molar flux
$\bar{N}_i^k$	$mol/(m^2s)$	species i segment k ordinary diffusion flux
Q_i^k	m^3/s	segment k feed flow rate of species i
s_w	m	W film thickness

continue...

Table C.1: List of variables and parameters

Symbol	*Units (and Value)*	*Description*
S	mm	distance between probes
t	s	time
t_s	μm	thickness of conductive film (Appendix B)
T	K	segment gas temperature
W	$0.025\ m$	segment side length
x_i^k		species i segment k mole fraction
z	m	1D segment coordinate
z_f	$0.0508\ m$	feed tube outlet location
ρ	$\mu\Omega m$	resistivity of conductive film (Appendix B)
ρ_i	kg/m^3	pure species gas density

BIBLIOGRAPHY

[1] Xia, L., P. W. Lee, M. Chang, I. Latchford, P. K. Narwankar, R. Urdahl, Chapter 11. Chemical Vapor Deposition, *Handbook of Semiconductor Manufacturing Technology*, Yoshi Nishi, Robert Doering, ed., New York: Marcel Dekker (2000).

[2] Wang, C. A., S. H. Gorves, S. C. Palmateer, D. W. Weyburne, and R. A. Brown, Flow visualization studies of OMVPE reactor designs *J. Crystal Growth* **77** 136-147 (1986).

[3] Moffat, H. K. and K. F. Jensen, Three-dimensional flow effects in silicon CVD in horizontal reactor, *J. Electrochem. Soc.* **135**, 459-471 (1988).

[4] Kleijn, C. R., Th. H. van der Meer, and C. J. Hoogendoorn, A mathematical model for LPCVD in a single wafer reactor, *J. Electrochem. Soc.* **136**, 3423-3433 (1989).

[5] Gadgil, P. N., Optimization of a stagnation point flow reactor design for metalorganic chemical vapor deposition by flow visualization *J. Crystal Growth* **134** 302-312 (1993).

[6] Kobayashi, A., A. Sekiguchi, K. Ikeda, O. Okada, N. Hosokawa, Y. Tsuchiya, and K. Ueno, The deposition rate for Cu CVD. In Advanced Metalization and Interconnect Systems for ULSI Applications, ed. by R. Havemann, J. Schmitz, H. Komiyama, and K. Tsubouchi, Mater. Res. Soc. Pittsburgh, PA, 177-183 (1997).

[7] Kim B. N. and H. H. Lee, Numerical simulation of metalorganic chemical vapor deposition of copper in a single-wafer reactor *J. Electrochem.Soc.* **144** 1765-1773 (1997).

[8] Moslehi, M. M, C. J. Davis, and R. T. Matthews, Programmable multizone gas injector for single-wafer semiconductor processing equipment, United State Patent 5,453,124 (1995).

[9] van der Stricht, W., I. Moerman, P. Demeester, J. A. Crawley and E. J. Thrush, Study of GaN and InGaN films grown by metalorganic chemical vapor deposition, *J. Crystal Growth* **170**, 344-348 (1997).

[10] Yang, C., C. Huang, G. Chi and M. Wu, Growth and characterization of GaN by atmosphere pressure metalorganic chemical-vapor deposition with a novel separate-flow reactor, *J. Crystal Growth* **200** 39-44 (1998).

[11] Theodoropoulos, C., T. J. Mountziaris, H. K. Moffat and J. Han, Design of gas inlets for the growth of gallium nitride by metalorganic vapor phase epitaxy, *J. Crystal Growth* **217**, 65-81 (2000).

[12] Moslehi, M. M., C. J. Davis, and A. Bowling, *TI Technical Journal*, Sept-Oct, 44-64 (1992).

[13] Stuber, J. D., I. Trachtenburg, and T. F. Edgar, Design and modeling of rapid thermal processing systems *IEEE Trans. Semicond. Manuf.* **11** 442-457 (1998).

[14] Kiether, W. J., M. J. Fordham, S. Yu, A. J. S. Neto, K. A. Conrad, J. Hauser, F. Y. Sorrell, and J. J. Wortman, Three-Zone Rapid Thermal Processor System. Proc. 2nd Int (1994). RTP Conf., 96-101.

[15] Theodoropoulou, A., E. Zafiriou, and R. A. Adomaitis, Inverse model based real-time control for temperature uniformity of RTCVD, *IEEE Trans. Semicond. Manuf.* **12**, 87-101 (1999).

[16] Christofides, P. D., *Nonlinear and Robust Control of PDE Systems: Methods and Applications to Transport-Reaction Processes,* Birkhauser Pub.Co. (2001).

[17] Banks, H. T., S. C. Beeler, G. M. Kepler, and H. T. Tran, Reduced order modeling and control of thin film growth in an HPCVD reactor, *SIAM J. Appl. Math.* **62** 1251-1280 (2002).

[18] Kepler, G. M., H. T. Tran, and H. T. Banks, Reduced order model compensator control of species transport in a CVD reactor, *Optim. Contr. Appl. Meth.* **21** 143-160 (2000).

[19] Kepler, G. M., H. T. Tran, and H. T. Banks, Compensator control for chemical vapor deposition film growth using reduced-order design models, *IEEE Tran. Semicond. Manuf.* **14** 231-241 (2001).

[20] Ireland, P. J., High aspect ratio contacts: A review of the current tungsten plug process, *Thin Solid Films* **304**, 1-12 (1997).

[21] Arora, R. and R. Pollard, A mathematical model for chemical vapor deposition process influenced by surface reaction kinetics: application to low-pressure deposition of tungsten,*J. Electrochem. Soc.* **38** (5) 1523 (1991).

[22] Kleijn, C. R., Computational modeling of transport phenomena and detailed chemistry in chemical vapor deposition - a benchmark solution, *Thin Solid Films* **365**, 294-306 (2000).

[23] Kleijn, C. R., C. J. Hoogendoorn, A. Hasper, J. Holleman and J. Middelhoek, Transport phenomena in tungsten LPCVD in a single-wafer reactor, *J. Electrochem. Soc.* **138**, 509-517 (1991).

[24] Kleijn C. R. and C. Werner, *Modeling of chemical vapor deposition of tungsten films*, Basel; Boston: Birkhauser Verlag (1993).

[25] Gougousi, T., Y. Xu, J.N. Kidder, Jr., G. W. Rubloff, and C. R. Tilford, Process diagnostics and thickness metrology for the chemical vapor deposition of W from H2/WF6 using in-situ mass-spectrometry, *J. Vac. Sci. Technol. B* **18**, 1352-1363 (2000).

[26] Reid, R. C., J. M. Praunitz and B. E. Poling, *The properties of gases and liquids* (4th edition), New York, McGraw-Hill (1987).

[27] Adomaitis, R. A., Objects for MWR, *Comp. & Chem. Engng.* **26** 7-8, 981-998 (2002).

[28] Chen, J., and R. A. Adomaitis, An Object-oriented Framework for Modular Chemical Process Simulation with Semiconductor Processing Applications, Submitted for publication *Comp. & Chem. Engng.* (2004).

[29] Leusink, G. J., C. R. Kleijn, T. G. M. Oosterlaken, C. A. M. Janssen, and S. Radelaar, Growth kinetics and inhibition of growth of chemical vapor deposited thin tungsten films on silicon from tungsten hexafluoride, *J. Appl. Phys.* **72** (2) 490-498 (1992).

[30] Groenen, P. A. C., J. G. A. Holscher, and H. H. Brongersma, Mechanism of the reaction of WF_6 and Si,*Applied Surface Sci* **78**, 123-132 (1994).

[31] Joshi, R. V., V. Prasad, M. L. Yu, and G. Scilla, Non-self-limiting nature of silicon reduction of WF_6 in cold wall systems, *J. Appl. Phys.* **71** (3) 1428-1441 (1992).

[32] Chang, H. -Y., R. A. Adomaitis, J. N. Kidder, Jr., and G. W. Rubloff, Influence of gas composition on wafer temperature in a tungsten chemical vapor deposition reactor: Experimental measurements, model development, and parameter estimation, *J. Vac. Sci. and Tech.,B* **19** 230-238 (2001).

[33] Smith, R. C., N. Hoilien, J. Chien, S. A. Campbell, J. T. Roberts and W. L. Gladfelter, *Chem. Master.* **15**, 292 (2003).

[34] Wang, Q., G. Yue, J. Li and D. Han, *Solid State Communications* **113** 175 (2000).

[35] Choo, J. O., R. A. Adomaitis, G. W. Rubloff, L. Henn-Lecordier, and Y. Liu, Simulation-Based Design and Experimental Evaluation of a Spatially Controllable Chemical Vapor Deposition Reactor, *AIChE Journal*, accepted for publication (2004).

[36] Waits, R. K., Semiconductor and thin film applications of a quadrupole mass spectrometer, *J. Vac. Sci. Technol. A* **17** 1469-1478 (1999).

[37] Xu, Y., T. Gougousi, L. Henn-Lecordier, Y. Liu, S. Cho and G.W. Rubloff, Thickness metrology and end-point control in WCVD process with SiH4/WF6 using in situ mass spectrometry, *J. Vac. Sci. Technol., B* 20(6), 2351-2360 (2002).

[38] T. Gougousi, R. Sreenivasan, Y. Xu, L. Henn-Lecordier, J.N. Kidder, Jr., G. W. Rubloff, and E. Zafiriou, In-situ Sensing using Mass-Spectrometry and its use for Run-to-Run Control on a W CVD Cluster Tool, *Characterization and Metrology for ULSI Technology: 2000 International Conference*, Gaithersburg, MD, 26-29 June 2000, *AIP Conference Proceedings*, Melville, NY, 2001, vol. 550, pp. 249-253.

[39] Hasper, A., J. Holleman, J. Middelhoek, C. R. Kleijn and C. J. Hoogendoorn, *J. Electrochem. Soc* **138**, 1728 (1991).

[40] Sivaram, S., M. L. A. Dass, C. S. Wei, B. Tracy, and R. Shukla, Comparison of mechanical and microstructural properties of hydrogen and silane reduced

low pressure chemical vapor deposited tungsten film, *J. Vac. Sci. Technol., A* 11(1), 87-95 (1993).

[41] Broadbent, E. K., W. T. Stacy, Selective Tungsten Processing by Low Pressure CVD, *Solid State Technology* December 51-59 (1985).

[42] Chang, C.Y. and Sze, S.M. *ULSI technology* (McGraw-Hill, 1996), Chap. 8.

[43] McConica, C. M. and K. Krishnamani, *J. Electrochem. Soc.* **133(12)**, 2542 (1986).

[44] Cho, S., L. Henn-Lecordier, Y. Liu, G. Rubloff, In-situ mass spectrometry in a 10 Torr W chemical vapor deposition process for film thickness metrology and real-time advanced process control, *J. Vac. Sci. Technol., B* 22(3), 880-87 (2004).

[45] Kuijlaars, K. J., C. R. Kleijn, and H. E. A. van den Akker, A detailed model for low-pressure CVD of tungsten, *Thin Solid Films* 270, 456-461 (1995)

[46] Meyyappan(editor), M.,C. R. Kleijn, Chapter 4. Chemical Vapor Deposition Process (*Computational Modeling in Semiconductor Processing*) Artech House: Boston (1995).

[47] Schoonman, J., P. J. J. M. van der Put, *Kintetics and Characterization of Tungsten CVD Processes*, Jan Ammerlaan: Delft University Press, (1994).

[48] Oosterlaken, T. G. M., G. J. Leusink, G. C. A. M. Janssen, and S. Radelaar, The kinetics of tungsten deposition from the H2/WF6-mixture studied by in

situ laser Raman scattering, Conference proceedings *ULSI XI, MRS* 549-553 (1996).